# Design of the h=1 Central Region for the K=500 MeV Superconducting Cyclotron

E. Liukkonen and T. Antaya

## Introduction

A good central region for the MSU K=500 MeV Superconducting Cyclotron (SCC) has more stringent operating requirements than those for cyclotrons using conventional magnets. Good beam quality is desired for the large variety of particles and energies for which the K=500 MeV SCC would operate, both as a stand-alone accelerator and later as an injector to the K=800 MeV SCC.

Many of these requirements are illustrated in Figure 1. Part (a) shows the range of final energies of the K=500 MeV SCC as a function of the charge-to-mass ratio. For q/m ratios less than 0.322 the maximum energy is determined by the K=500 MeV bending limit of the cyclotron, while for larger q/m values $E_{max}$=q/m x $B_f$, where $B_f$=160 MeV is the sector focusing limit of this cyclotron.[1] Due to the $\nu_r + 2\nu_z$=3 resonance the lowest magnetic field which can be used is about 3.1 T. The corresponding minimum energies are plotted as a dashed line in Figure 1(2).

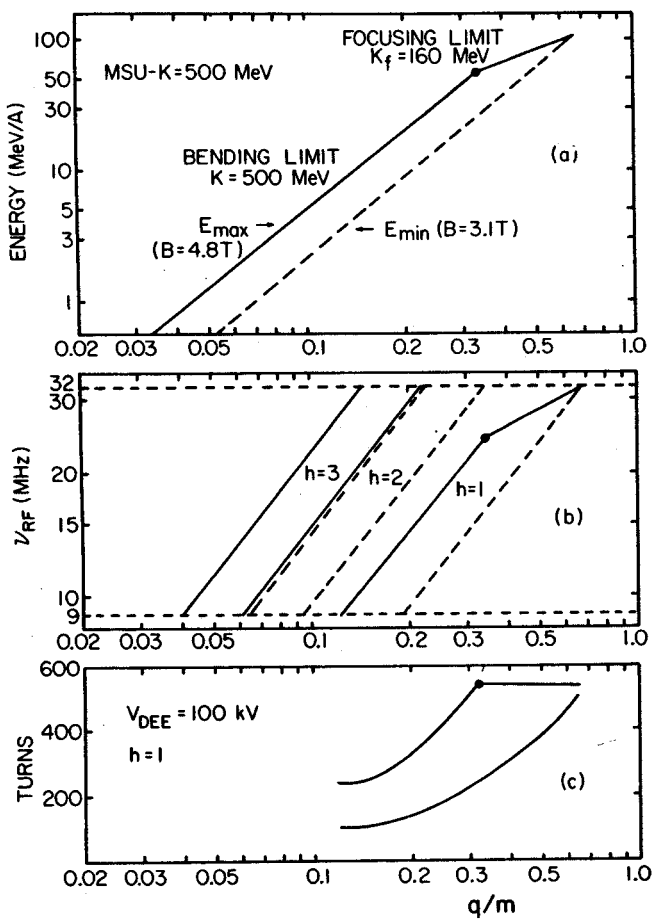


Fig. 1 (a) The maximum (solid line) and minimum (dashed line) energies which can be accelerated in the magnetic field of the K=500 MeV superconducting cyclotron. (b) The required rf frequencies in the h=1, 2 and 3 harmonic operations of maximum and minimum energies. (c) The range of number of revolutions in the h=1 acceleration if $V_{dee}$= 100 kV, as a function of charge-to-mass ratio, q/m.

The operating range of the radio frequency system affects the central region design too. During the earliest phase of development of the K=500 MeV SCC, a frequency range of 27-89 MhZ was considered, with cyclotron operation in third and ninth harmonic modes. When it was revealed that at such high frequencies a serious voltage gradient occurs along the physically large dees, and that the transit time effects are difficult to overcome for higher harmonics, it was decided to lower the rf - frequency range to the present 9-32 MhZ. Figure 1(b) shows the required rf-frequencies for the h=1,2 and 3 harmonic modes of operation at the maximum (solid line) and minimum (dashed line) final energies of the K=500 MeV SCC. The change in the slope of the h=1 maximum frequency line is due to the fact that $B_f$=160 MeV will be exceeded for these particles unless the magnetic field and frequencies are lowered. By comparing Figure 1(a) and 1(b) one sees that in stand-alone operation all particles with a minimum final energy greater than the Coulomb barrier (about 8 MeV/A) can be accelerated in the first harmonic mode. This is the reason why first harmonic acceleration has had the highest priority in our central region design studies.

The MSU K=50 MeV cyclotron operated with a fixed orbit geometry, and required only one central region for first harmonic acceleration. In order to minimize the orbital path length of particles in the cyclotron, the K=500 MeV SCC will instead use the highest dee voltage (100 kV) whenever possible. But a fixed dee voltage means a variable orbit geometry, with turn numbers ranging from 100 to 540 in the h=1 operation as can be seen in Figure 1(c). A single central region would not be able to fulfill all of these operating requirements. Since the ions with the highest energies and turn numbers will be the most difficult to accelerate the development of a high-energy, high-turn number central region naturally got top priority. The goal for the first central region of the K=500 MeV SCC was to design a central region which can be used to accelerate particles in first harmonic mode of operation with turn numbers ranging from 400 to 550 turns.

The black dot in each part of Figure 1 corresponds to the ion chosen as "model" particle for these design studies, q/m=0.322 (e.g. $^{28}Si^{9+}$). Several other particles have also been used in the design work, as the necessary magnetic fields are available. Their q/m values range from q/m= 0.042 ($^{238}U^{10+}$) to q/m=0.667 ($^{3}He^{2+}$), and their final energies correspond to the maximum energy limit in Figure 1(a). These magnetic fields

are realistic fields based on the measured fringe field and flutter, but they have been made mathematically isochronous for the desired particle. The fields have a magnetic field hump in the center of the cyclotron. These humps are calculated by requiring that $\nu_z$=0.1 for the radius of r<5 in.

A design of the first central region for first harmonic operation was completed in Autumn of 1978. It gave adequate overall clearances and reasonable beam properties but was unnecessarily restricted only to the highest turn numbers, and showed intolerable distortions in the radial phase space motion. By advancing through a succession of improvements of that central region we have now reached a final design that meets the goals outlined above but without any of the limitations. This new design will be presented in this progress report.

## 2. Electrolytic Tank Measurements of the Electric Fields

The K=500 MeV SCC will accelerate ions with 3-dee and 3-dummy dee electrodes, each 60° wide. Where the dees come together at the center of the cyclotron the resulting electric field is quite complex. The dees are so "thin" in azimuth that there will be practically no electric field free region in the first few revolutions. An electric field like this cannot be accurately modeled analytically, yet it is still desirable to perform realistic orbit calculations in the central region of the cyclotron. Hence all realistic orbit calculations must be based on measured electric fields. In the development of the h=1 central region for the K=500 MeV SCC measurements of central region electric fields have played an essential role.

The electric field information can be most conveniently obtained using an electrolytic tank model. A system has been developed at MSU to automatically measure a rectangular lattice of potential differences of a scale model of an electrode structure. The present facility, shown in Figure 2, is a modernized version of the original MSU electrolytic tank facility as reported by Reiser and Kopf in Ref. 2). A measurement probe mounted on a motor driven milling machine table, whose motion provides for the automatic field scanning in rectangular coordinates, served as the basis of the old facility and continues in that capacity. In the new set up interface circuits provide for direct computer control of the mill. It is connected to a PDP 11/20 mini computer through a serial data transfer line, through which BCD-coded position, control and voltage data can be transfered to and temporarily stored on a floppy disk. The data can be transfered to the main laboratory computer after the run is complete.

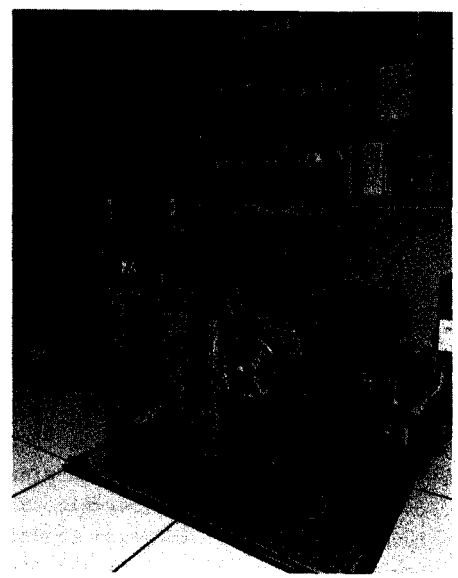

Fig. 2 A photo showing the electrolytic tank facility.

Figure 3 shows schematically the information flow paths in the present electrolytic tank facility, affectionately known as "Fish Tank". It should be noted that the probe scans continuously in one dimension (y) but moves stepwise in the other (x). After completing a particular y scan, the probe returns along the same line and scans it in the reverse direction. The data for each of these scans are labelled separately. This procedure eliminates the backflash of the mill. The position and movement of the probe is controlled by a chain of electrical pulses orginating from coding units in the shafts of the mill. The x-axis coder is a slotted circular plate which rotates as the shaft turns, chopping light from two light bulbs shining on photo detectors. The y-axis coder is a commercial coder of the capstan type. The minimum controllable step length is 0.01 inches, but in practice the shortest applicable step length has proved to be 0.04 inches.

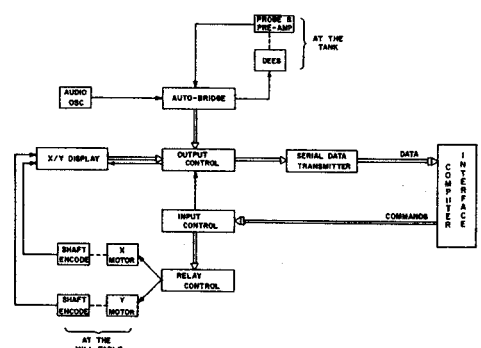


Fig.3 Information flow schematic for the electrolytic tank facility.

The electrodes in the tank are connected to a voltage source and an automatically balancing bridge with a voltage probe measures the resulting potential difference. Reiser and Kopf determined that adverse surface polarization of the water could be reduced by using an ac voltage. Any frequency in the range from 400 to 1500 Hz is acceptable, but the buildup of stray capacitances in the tank at higher frequencies limits accuracy. We have used a 500 Hz ac voltage source with a peak-to-peak amplitude of about 3 V.

The probe consists of a 0.5 mm diameter stainless steel wire maintained in an insulated sleeve. The probe height is adjusted so that it just touches the upper surfaces of the electrodes. This height corresponds to the median plane of the cyclotron. Hence the electrolytic tank model must be level with all median plane electrodes at the same height. In this configuration the water level is not very critical as long as it remains above the tops of the electrodes. (To increase the conductivity of the water a few drops of liquid soap is added).

The accuracy of the system was checked by measuring the voltage distribution of a parallel plate conductor, for which the potentials can be computed. This test gave an error of one part in one thousand, which incidently is sufficient to study also the vertical motion, where one needs to obtain second derivatives from the median plane voltage data (see a separate discussion on the vertical motion in the central region in this annual report by Gordon and Liukkonen).

The electric fields used to study the h=1 central geometry were obtained by voltage measurements in an 11 in. diameter circular electrolytic tank. In most cases the electrode structurees in the tank were full scale models of the central region. Data were normally taken in a square mesh of 140 by 140 points in 0.04" steps. Such measurements take about 7.5 hours.

The three dees and dummy dees of the K=500 MeV SCC are represented by copper plates set 0.5 inch below the median plane level to correspond to a 1.0 inch dee gap. As is customary, the mirror image of the dee structures above the median plane was omitted. All other central region penetrations were cut at the median plane too. This greatly simplifies the model fabrication and data taking. Placing the water level just above the dee tip posts then defines the median plane of the tank, and imposes the proper boundary conditions on the electrodes. The latest version of the h=1 central region geometry for the K=500 MeV SCC is shown in Figure 4. The finger points to the puller electrode. This is the version which will be discussed in this report.

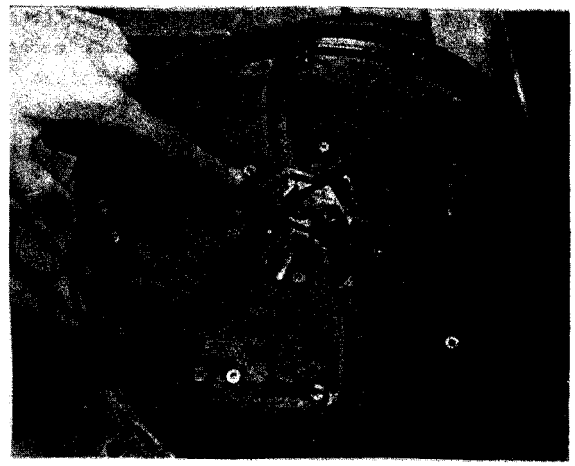

Fig. 4 A photo of the latest (July 1979) tank model of the central region which is designed for the high turn number and high energy h=1 acceleration.

In h=1 and h=2 modes the three dees of the K=500 SCC will operate with 120° phase shifts. Therefore one has to know the spatial electric field distribution separately for each dee. This can be achieved by making three electrolytic tank measurements. In each measurement the voltage is applied to only one dee, with all other dees and dummy dees grounded.

Figure 5 shows the equipotential contour maps from three such measurements carried out on the model in Figure 4. In the orbit calculations the potential values and electric field components of the three maps will be superimposed with appropriate time factors to produce the total potential and electric field components at any desired location in the central region.

Figure 6 shows a median plane equipotential contour map of the same central region as in figures 4 and 5. In this case the potentials for all three dees have been combined. This corresponds to the h=3 acceleration mode in which all three dees are in phase. In Figure 6 the actual shapes of the dees, dummy dees, electrodes and the ion source have been superimposed on the contour map. All acceleration gaps except the source-puller gap are 0.5 inches wide. The gap between the grounded ion source and the puller electrode on the end of the first dee is 10 mm, which should be adequate to hold the 100 kV rf voltage.

### 3. Source-puller Calculations

Due to the high magnetic field of the superconducting magnet, one can expect that the transit time between the ion source and the puller will become a serious limiting factor in the design and operation at the K=500 MeV SCC. As a result, the properties of source-puller trajectories were studied in some detail.

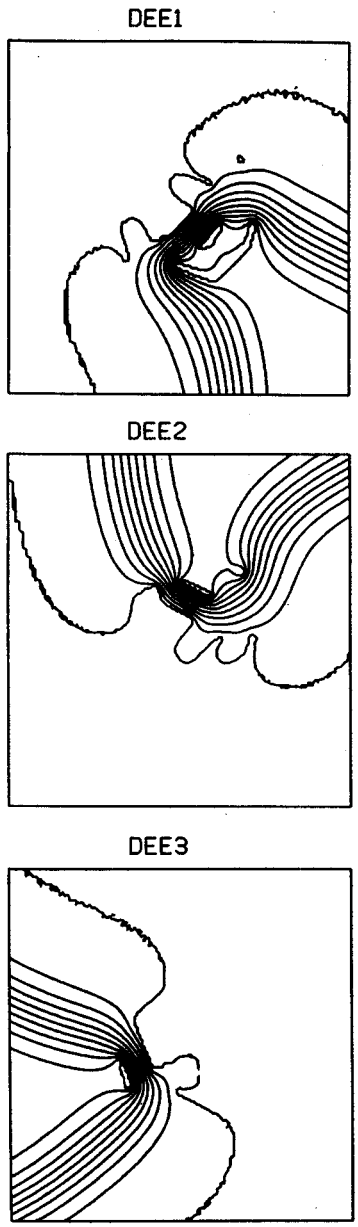


Fig. 5 Three equipotential contour maps representing electric fields of each dee of the tank model shown in Figure 4.

A two-dimensional electrolytic tank model in 6:1 scale of the source-puller region was built, and an electric field map measured. In this model two circular electrodes in front of the ion source formed the puller electrodes. The ion source slit was recessed at an angle of 30° approximately 0.5 mm into the surface of the ion source. This same recess was used for many years in the ion sources at the MSU K=50 MeV cyclotron. The median plane aperature of the slit was 60mils (approximately 1.5 mm). The minimum surface-to-surface distance between the ion source and puller electrodes was set at 10 mm to hold the required 100 kV dee voltage. A

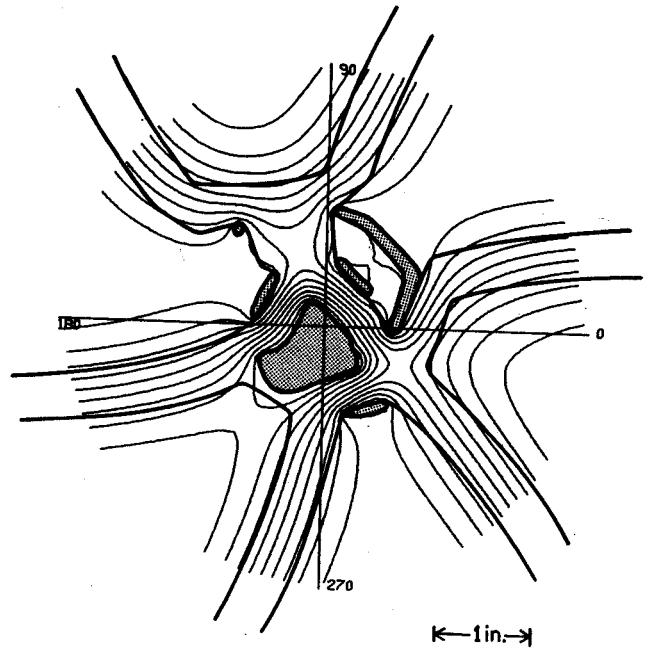


Fig. 6 In this figure the three separate electric fields of Figure 5 are combined and shown together with the actual shapes of dees, dummy dees and other electrodes. The structures penetrating the median plane are shadowed.

special feature in this design is that the puller electrode on the left side is closer to the ion source in order to allow for more bending in the high magnetic field of the SCC. The geometry and measured voltage distribution as an equipotential contour map can be seen in Figure 7 together with a few ion trajectories for the q/m=0.322 particle. These trajectories were used in the radial phase space study of the central region which is described in a later section of this report.

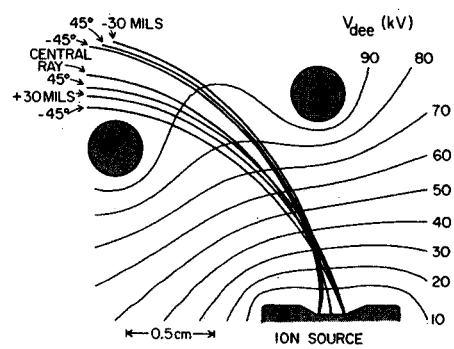


Fig. 7 Ion source-puller geometry which was used in the design calculations. Shown are also equipotential lines ($V_{dee}$=100 kV), the central ray and three trajectories starting at each edge of the exit slit. The aperature of the ion source slit is 60 mils (appr. 1.5 mm), and the slit is recessed about 0.5 mm at a 30° angle below the face of the ion source. The minimum distance between the ion source and puller is 10 mm. Starting energy of ions and angular divergence of ions were 10 eV/nucleon and ±45°, respectively, corresponding to an emittance of 1 mm·mrad at the extraction radius.

It is very difficult to construct a realistic source-puller model for two reasons. First, the mechanism of ion extraction from an arc plasma is not yet completely understood. Second, the inclusion of the space charge effect in orbit calculations using the model electric field is a very complicated task. Our calculations have then omitted the influence of the space charge, and the shape of the plasma boundary. These aspects of the acceleration problem certainly can play an important role in modifying the focusing properties of the field, but one can assume that the central ray trajectory remains unaffected. Figure 7 shows the central ray and three trajectories starting at each edge (± 30 mils). The center ray of these extreme groups exits perpendicular to the face of the ion source, while the other two exit at $\pm 45^{\circ}$ angles to the normal direction. (The $\pm 45^{\circ}$-rays that go with the central ray have been omitted from the figure to improve clarity). Each ion has a starting energy of 10 eV/nucleon. The initial angular divergence ($\pm 45^{\circ}$) and the starting energy were chosen to give a radial emittance of approximately 1 mm.mrad at the extraction radius. The central ray starts at $240^{\circ}$, which is $30^{\circ}$ before maximum negative voltage on the first dee (the puller electrodes being connected to the first dee).

The other rays have slightly different starting times as will be explained later (see the radial phase space section). Figure 7 dramatically shows how strongly the recessed slit of the ion source focuses the particles. In a real machine, the overfocusing, as shown in Figure 7, would be greatly damped by ion source dynamics previously mentioned. These results confirm a source-puller study done by M. Reiser[3] at MSU in conjunction with the design studies for the MSU K=50 MeV cyclotron.

In Figure 8 the kinetic energy and the transit time (in rf degrees) are plotted for q/m=0.322 particles as a function of the starting phase in the h=1 acceleration. The highest energy is obtained when particles start at $\tau_0=210^{\circ}$, 30 rf degrees after the rf voltage changes sign ($V=V_0 \sin\tau$ for the first dee). Although this high energy gain would be a very desirable feature the starting phase $\tau_0=210^{\circ}$ is far too early, since the intensity of the beam is proportional to $V^{3/2}$ and high intensity is also desirable. Therefore one has to make a compromise between energy gain and intensity: we have selected $\tau_0=240^{\circ}$ for h=1 ($\tau_0=230^{\circ}$ for h=2 and $\tau_0=220^{\circ}$ for h=3). Figure 8(b) shows in rf degrees the time required for particles to reach the line between the centers of two puller electrodes. It is about 80 degrees for $\tau_0=240^{\circ}$, and is fairly constant for all particles with $\tau_0=240^{\circ}\pm 30^{\circ}$.

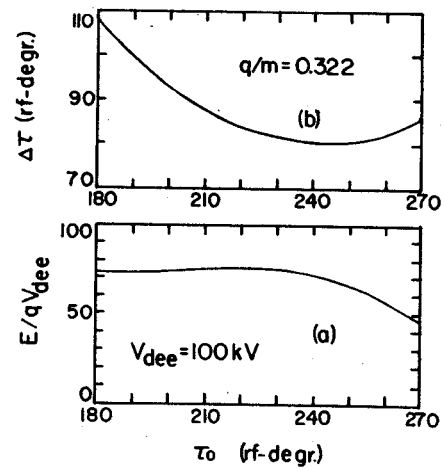


Fig. 8 (a) Energy gain in the gap between the ion source and puller as a function of the starting phase for the q/m=0.322 particles in h=1 acceleration. (b) Transit time from ion source to puller (time convention: the voltage of the puller electrode is $V=V_{dee}\sin\tau$).

Figure 9 shows the energy gains and transit times of different particles as a function of charge-to-mass ratio for h=1, 2, and 3 accelerations, for the above selected starting time. The required rf frequencies of the K=500 MeV cyclotron for maximum energies, are also repeated. As one can see, the 9-32 MHz frequency range is very nicely matched to the transit time effect. There are practically no limitations in the h=1 and 2 operations, while in the h=3 mode of operation, the transit time effect only prevents the use of the highest frequencies with q/m between 0.12-0.145. In all cases there is a large frequency overlap between the adjacent harmonics.

Figure 10 shows more demonstratively a few typical source-puller trajectories in the maximum magnetic field of the K=500 MeV SCC for different particles, specified by their charge-to-mass ratio q/m, and for starting times representing the central rays. In the h=1 case all particles clear the puller easily, but in the h=2 and 3 modes of operation the particles with higher q/m-ratios are bent back before reaching the puller.

A feature worth noting is that in the h=1 mode of operation (see Figure 9(c) the transit times are nearly constant for $q/m \geq 0.3$. This is due to the fact that focusing limit of the K=500 MeV SCC forces the use of lower magnetic field for these particles at highest energies (see Figure 1(a).) Therefore trajectories of these particles are nearly identical. This allows the design of a central region for those particles with a fixed source-puller geometry in the h=1 operation, which greatly simplifies the construction and operation of the cyclotron.

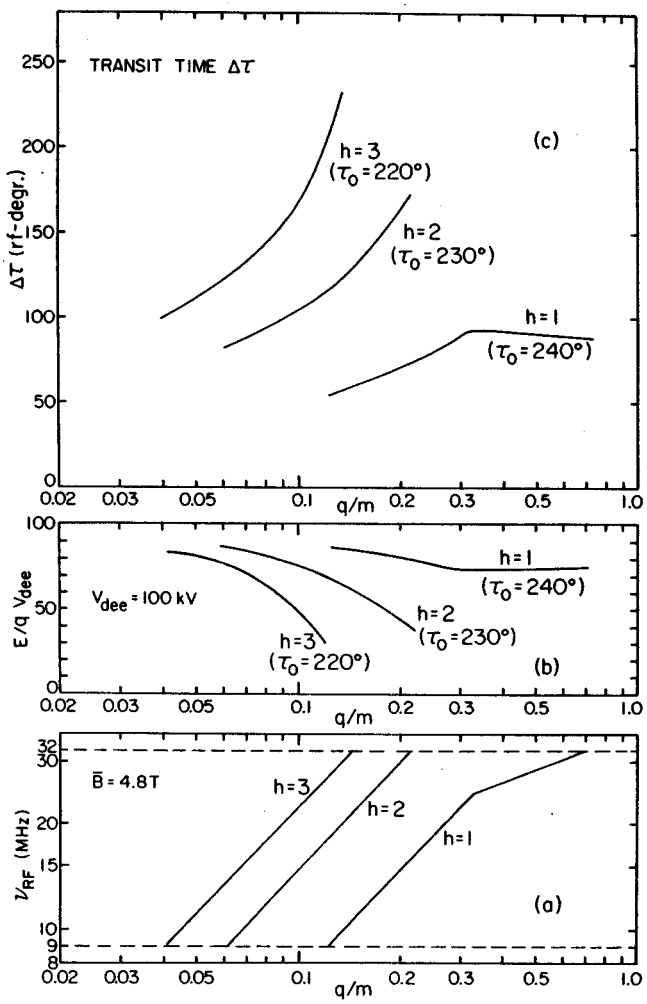


Fig. 9 (a) The required rf frequencies, (b) the energy gain and, (c) the transit times in the gap between the ion source and puller are plotted as a function of charge to mass ratio, q/m for the first, second and third harmonic acceleration of particles in the 500 MeV cyclotron operating with the maximum magnetic field.

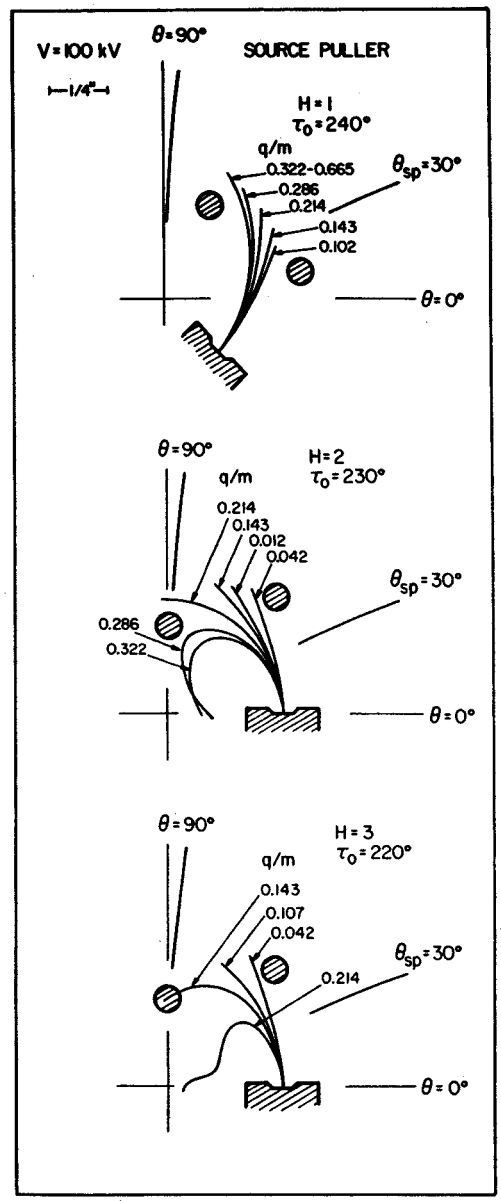


Fig. 10 Ion trajectories between the source and the puller for the h=1, 2 and 3 harmonics in the maximum magnetic field of the 500 MeV superconducting cyclotron. $\theta_{sp}$ denotes an acceleration gap at a spiral angle of $\theta_{sp}=30^{\circ}$.

## 4. Central Region

The first central region studies for the K=500 MeV SCC were made in 1977 for the third harmonic mode of operation, when the 27-84 MHz rf frequency range was under consideration. An electrolytic tank model was built and a complet set of electric field maps was measured. This electric field served as a first approximation on which all later models are based.

The introduction of the lower rf frequency range naturally shifted the design efforts to a central region suitable for the h=1 acceleration. Orbit calculations using the revised CYCLONE program[4] showed however, that the basic central geometry was not well matched for the h=1 beams. Only a marginal clearance was left between the ion source and dees for holding the required dee voltage of 100 kV. A special effort was made to overcome the clearance problems. A new electrolytic tank model was designed, where the dummy dee between dees no. 1 and no. 2 was cut shorter to allow locally higher energy gain and subsequently higher radial gain 180° later where it was urgently needed (see Figures 4 and 6). The tank model was built and measured. The calculations were repeated, showing that the new design had a desirable effect: the overall clearance was reached. This central region however was unnecessarily restricted to the highest turn number cases (around 540 turns). It also produced a serious distortion in the radial phase-space motion. To improve the design a chain of modifications were made advancing step by step to the final configuration, which is shown in figures 4 through 6. In each step an electrolytic tank model had to be built and measured, and then

extensive orbit calculations performed. Figure 11 shows the central-ray orbit of the q/m=0.322 particles calculated using the latest design of the central region. An equipotential contour map is also superimposed in the same figure. The case shown corresponds to 540 total revolutions in the cyclotron. The position of the ion source was determined so that the beam is well centered after few revolutions, and that the phase of particles will approach to zero after about 20 revolutions. A typical phase history of the q/m=0.322 particles is plotted in Figure 12 as a function of the turn number. A large positive phase in the beginning of the acceleration is due to the magnetic field hump in the center of the cyclotron. This magnetic hump contributes to the axial focusing with $\nu \simeq 0.1$ during the first revolutions. (For the vertical motion in the central region, see a separate contribution in this Annual Report by Gordon and Liukkonen).

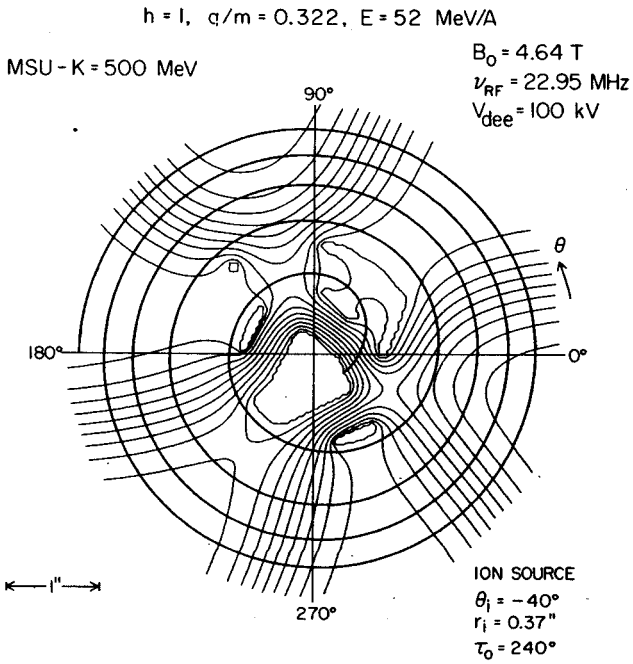


Fig. 11 Central-ray orbits of the q/m=0.322 particles which can be accelerated to the maximum energy of 52 MeV/A in the K=500 MeV cyclotron.

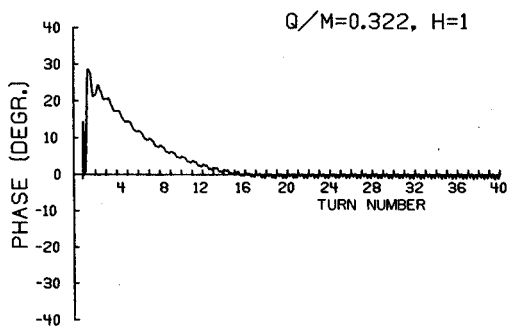


Fig. 12 Phase of the central-ray particles of Figure 12 as a function of turn number.

The latest h=1 geometry was also studied using $^{14}N^{4+}$ (q/m=0.286; E=41 MeV/A) and $^{2}H^{1+}$ (q/m=0.498; E=81 MeV/A) beams. Both of these particles produced well centered beams with the same starting conditions as indicated in Figure 11. The lowest dee voltage which can be used is a little above 90 kV. The lowest turn number case was studied by increasing the dee ovoltage. A dee voltage of 135 kV which corresponds to 400 turns, still clears all electrodes, thus completing our design goals.

## 5. Radial Phase Space Studies

Previous sections have outlined the major design features for the h=1 harmonic central region, whose ultimate performance will have to be determined by the quality of accelerated beams. Some properties can however be inferred in advance by studying beam-like bundles of ion trajectories that traverse the model electric field. In this section orbit characteristics derived from extensive studies of the radial phase space $(r,P_r)$ of such trajectories will be presented. The results indicate the sensitivity of the radial phase space to the electric field configuration at the beginning of the acceleration process.

In many studies of the model central region it is only necessary to look at properties of the central ray trajectory. (This orbit begins at the center of the ion source slit and emerges perpendicular to the face of the ion source). In this way the model can be adjusted to improve clearances, orbit centering and other beam properties but provides little information about the expected beam quality. In an effort to confirm that the general design criteria are adequate, a group of orbits leaving the ion source at different locations and angles were computed so that the effects of the central region on the radial phase space could be studied. As will be shown the beam is especially sensitive to the central electrode configuration, particularly in the region between the ion source and the puller electrode. This is true because the accelerating ions are still travelling at low velocity, and small changes in the electric field can cause significant changes in ion trajectories. For example the size of the ion source opening determines the initial radial spread of the beam. Different ions in this initial beam will travel slightly different trajectories, and will have slightly different transit times, energy gains and phases ($\phi=\omega t-\theta$) after traversing the source-puller region. The number of these effects to survive depends upon the focusing and defocusing actions of the central electrode geometry.

The computer program CYCLONE was used to study the radial phase space of the central region

which is shown in figures 4 through 6. The ion chosen for the study was again q/m=0.322, which lies near the magnetic focusing and bending limits of the K=500 cyclotron for first harmonic operation (see Figure 1). With CYCLONE a bundle of nine accelerated rays were tracked from the ion source slit through the central region of the cyclotron to a radius of about 7 inches. The starting conditions are described in a previous section and illustrated in Figure 7. The central ray starts at 240°, which is 30° before maximum voltage on the first dee (that bears the puller electrode). The other rays have starting times adjusted so that after a few turns there remains only small residual differences in phase and energy gain per turn between the rays. These rays have starting times grouped about the central ray in an interval of about 8°. With these starting conditions it is found that after 40 revolutions the energy gain per turn varies by only 1 part in $10^5$ for extreme rays in the bundle and the phase spread is only about 0.2°. In this way the longitudinal phase space ($E,\phi$) was effectively decoupled from the radial phase space, so that purely radial effects could be considered.

Figure 7 dramatically shows the effects of the source-puller configuration on the orbit trajectories. The recessed slit strongly focuses the rays. In Figure 13 the extreme trajectories (+30, -45; -30, +45) are plotted with the region between them shaded in. In this figure the maximum radial spread of the trajectories is about 5 mm. This provides an estimate of the radial spread of the accelerated beam. Note that it should also be possible to test these calculations by looking for fat and thin beam spots in the first few turns.

The evolution of the radial phase space during the first two revolutions of the cyclotron is shown in Figure 14. The phase space is plotted at selected azimuthal angles in the coordinate system of the central region. Momentum is plotted in cyclotron units, $P=P/M_0\omega_0$ where $\omega_0$ is the cyclotron frequency of this ion. The figures were constructed by plotting ($r,p_r$) plots for all nine rays and then closing the region between the points to approximately conserve the area according to Liouville's theorem. The point (+30 mils, +45°) is indicated by the large closed circle and the motion of the central ray by a dashed curve. The increasing radial spacing of the curves for the equal angles ($\theta$= 30,60,90°) shows the radial gain of the ions through acceleration. In this way the bunching of curves in the region 60-180° on the first turn is a direct result of the fact that the beam is most out of phase with the accelerating voltage in this region. The change in the tilting of the figures reflects the focusing and defocusing effects

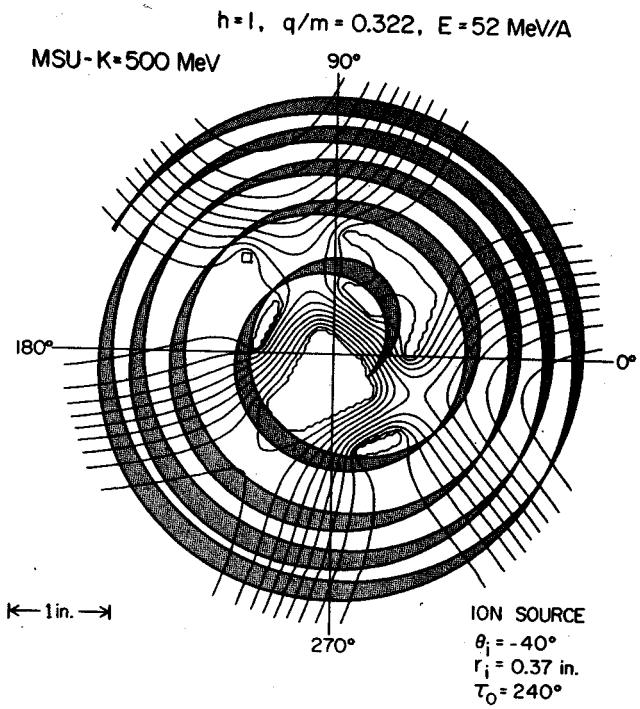


Fig. 13 The extreme trajectories of the q/m= 0.322 particles, with the area between them shadowed, starting at extreme edges of the ion source slit and ±45° divergence. The initial energy (10 eV/A) and divergence of ions was selected to correspond to the emittance of 1 mm mrad at the extraction energy.

in the central region, which makes the extreme rays (±30 mils) precess around the central ray. The elongation of the curves is caused by the over-focusing in the source-puller electric field.

The two main features of this graph are that no radial blow-up of this group of rays is observed and that the phase space area is fixed in all essential characteristics by θ=270° on the first turn. The figures change as the trajectories passes through the source-puller region until relative stability is achieved by θ=270°. The inset shows that the area on the second turn has not much changed by the tenth turn, by which time the central electrodes have long since been cleared. Central region studies at MSU for the K=50 MeV cyclotron obtained similar results[3], though they did not go as far as directly examining the radial phase space. Since the K=50 MeV cyclotron central region achieved remarkable success there is no reason to expect otherwise for the K=500 MeV. These same studies also showed that an ion source with a shallower recess would reduce the over-focusing in the source-puller region, but due to the neglected space charge effects the optimum choice would be somewhere in between.

## 6. Conclusion

Design work for the h=1 central region, which is reported in this progress report, has achieved

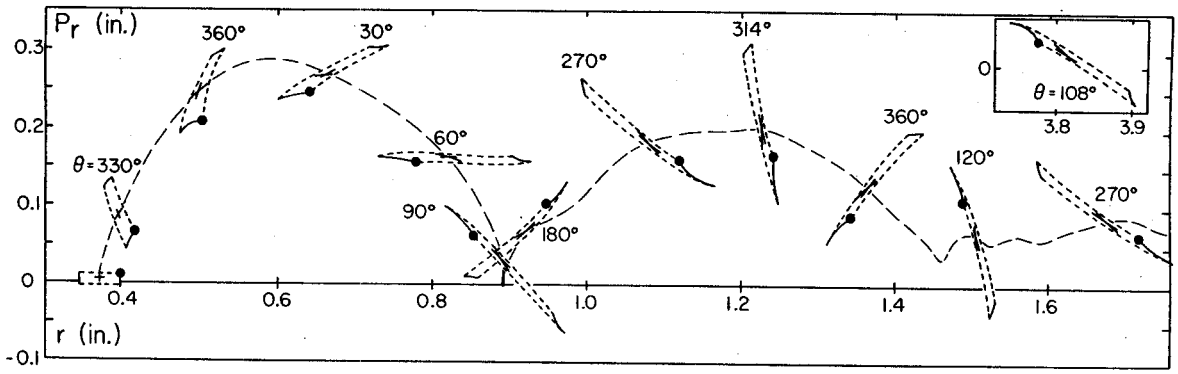


Fig. 14 A radial phase space plot of the q/m=0.322 particles starting with a rectangular shape from the ion source. For details, see text.

most of the goals set in the beginning of the work. The highest turn number case with 540 revolutions in the maximum magnetic field of the K=500 MeV SCC can clear all supporting structures of the central electrodes with adequate clearances. All beams with q/m 0.28 and turn numbers from 400 to 560 are well centered after leaving the central region of the cyclotron. A fixed ion source geometry is possible for all of these beams. Despite the complex electric field during the first few revolutions, the radial phase space behaviour of the beam is reasonably smooth.

There are still many details which have to be studied before the design work is completed. One has to study the behaviour of many spurious beams which could accelerate in the same field and frequency as the desired beam, since one wants to stop spurious beams as soon as possible. The sensitivity of the accelerated beam to the source-puller electric field also manifests more studies. Finally one has to complete the radial phase space study by including the finite energy and phase spread in the calculations. This information is especially needed in designing the radial phase slits.

1. H.G. Blosser and D.A. Johnson, Nucl. Instr. and Meth. 121(1974)301.
2. M. Reiser and J. Kopf, Rev. Sci. Instr. 36(1965)1022.
3. M. Reiser, MSUCP-16(1963).
4. M. Gordon, S. Motzny, and J. Bishop, MSU Annual Report 1977-1978.

# Ion Source Experiments in the Superconducting Magnet

M.L. Mallory

During the past year the superconducting magnet was utilezed as a heavy ion source test facility. Fig. 1 shows a charge state distribution measurement from the Penning heavy ion source with nitrogen gas. The charge state distribution is similar to data obtained at low magnetic field.

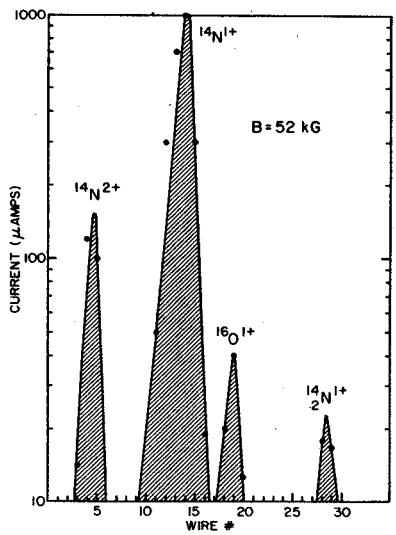


Fig. 1. The charge distribution of nitrogen gas in a Penning heavy ion source at 5.2T. The higher charged ions are detected when the magnetic field is 3.7T. The charge distribution at high magnetic field is similar to results obtained at low field values.

The theoretical understanding of ion formation from the Penning heavy ion source, e.g. Fig. 1, cannot be successfully described by a single electron impact theory, but a good fit to the data is obtained by an assumption of single and multiple electron impact. Fig. 2 shows a modification to the Penning heavy ion source that was made with the intent of enhancing possible electron multiple impact collisions. This modification allows a voltage potential well for the positive ions. With the application of > 10 volts on the electrode, a change in the charge distribution was detected, but surprisingly the lowest charge state was enhanced. (See Fig. 3.)

The following model is proposed to account for the above observation. The positive ions are formed in the ion source chimney and are confined to helical paths about the magnetic field lines. The ions drift up and down the magnetic field lines toward the cathodes and as they approach the cathodes are accelerated by the arc voltage; they then collide with the cathodes and are assumed to be lost. The observation that low charged ions have a greater loss probability leads to the proposal that they have a higher average velocity distribution than highly charged ions. The charge state distribution detected with the potential well source is a better sample of the ion formation process than previous charge distribution measurements, and it more closely approximates the single electron impact model. In the single electron impact model, no change in charge distribution as a function of magnetic field is expected.

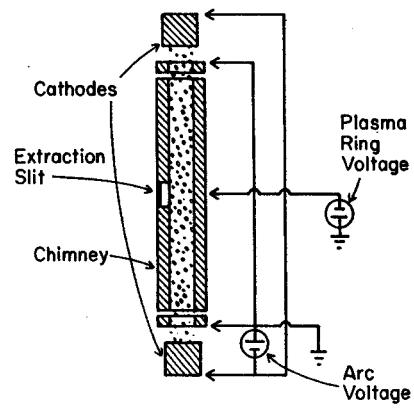


Fig. 2. A modification to the Penning ion source that allows plasma trapping experiments. The plasma voltage ring was operated at both positive and negative voltages and charge distribution measured in all cases.

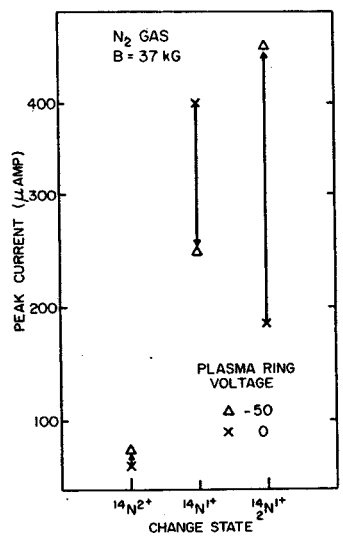


Fig. 3. The change in charge distribution for three ions of nitrogen. The trapping of the plasma greatly enhanced the intensity of the molecular ion of nitrogen. This charge distribution more closely resembles the theoretical results of single electron impact.

In summary, the ion source performance in high magnetic fields appears to be the same as at low field and therefore accelerator beam performance can be estimated from existing cyclotron results. Secondly, a beam loss process has been detected from the source and this process has not been considered in past charge distribution measurements.

# Centering of the Coil and the Cryostat in the K500 Magnet

P. Miller, D. Johnson, H. Blosser, D. Poe, H. Laumer, and G. Stork

The coil and the iron cryostat can be moved independently with respect to the yoke. If either structure is offset from the center axis of the yoke the magnetic field will be unsymmetrical, expressed quantitatively by the first harmonic term in the Fourier series expansion of the mid-plane magnetic field. The magnitude of the first harmonic is approximately equal to the product of the centering error and the radial derivative of the average field produced by the structure that is off center. The phase angle is either in the direction of the centering offset or opposite to it, according to whether the radial derivative is negative or positive.

## 1. Centering Coil and Tank by Harmonic Measurements

The radial distribution of the first harmonic created by displacements of the coil and the tank were determined experimentally by making a known displacement and subtracting the first harmonic vectors (magnitude and phase) measured in maps taken before and after the coil or tank was moved. These form factors are plotted in Fig. 1. A negative value implies a phase shift of 180° between the displacement and the resulting first harmonic (radial derivative is positive). Note that the tank form factor contains a contribution due to the coil because the coil moves with the tank. It is not necessary to subtract this since the tank and the coil form factors are distinct and independent in the large radius region (r > 20") where fitting is done. These two components then are directly related to the mechanical devices for moving the coil and the tank.

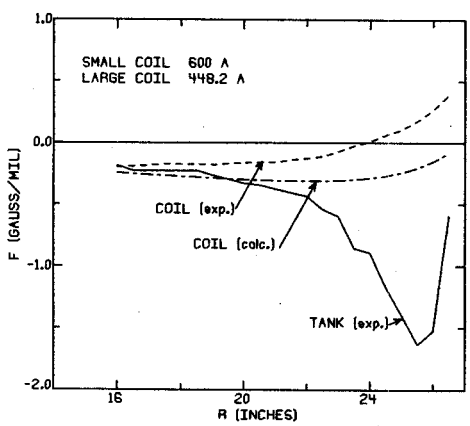


Fig. 1. Radial form factor (F) of the harmonic amplitude due to centering error or deformation of coil and tank structures in the K500 magnet. The calculated coil form factor (dot-dash curve) represents the radial derivative of the total air core coil field. The experimental curves were inferred by subtraction of first harmonic vectors at corresponding radial positions in maps measured before and after a known displacement was made. The experimental form factors were used in the fitting procedure for centering the coil and the tank.

A centering error produces a horizontal magnetic force which must be balanced by the supports. In the case of the coil this force can be measured, since the support links contain strain gauges. This condition serves as a check of the centering inferred by analysis of field maps. The goal of the centering program is to minimize the total magnetic force on the coil, which has been achieved. The forces on the coil tank cannot be measured. It will be dowelled to keep it in place at the cencentered location after all shimming and machining of iron is completed.

The analysis assumes that the first harmonic is entirely due to a centering error of the coil or the tank. In fact, there is a first harmonic of about 4 or 5 gauss over most of the machine which appears to be due to a misalignment of the poles or other iron structures. Attempts to cancel this with the coil or tank will give different results depending on the fitting interval. The centering was stopped when the condition shown in Fig. 2 was achieved, with a first harmonic below 2 gauss over the outermost half inch of the mapping grid. In this condition the magnetic force on the coil is small, corresponding to a centering error of 2 mils (discussed in Section 2).

The first harmonic has a peak (magnitude 8 gauss) near the joint in the pole tips at r = 14 inches; elsewhere the magnitude is 3-5 gauss except outside of 25 inches and inside of 1.5 inches, where it becomes smaller. The phase angle follows the pole tip spiral from r = 3 inches to 15 inches. At larger radii it deviates from it markedly. We interpret these data to mean that the first harmonic has at least two sources: 1) the inner section (r = 3 to 14 inches) of one pole is skewed. 2) The other source is something other than a spiral pole tip, such as the yoke or the sector bars attached to the cryostat. The first component has a decreasing phase which tracks the pole tip spiral (see Fig. 2).

A contour map of the magnetic field with the average field and the 3n-symmetry harmonics subtracted was prepared to look for deviations from the desired symmetry. One feature that appears is an apparent rotation of the inner portion of one sector spiral, as indicated by twisting the contours. This supports the given interpretation of the first harmonic data.

## 2. Coil Centering by Balancing Forces in Support Links

The forces on the three radial coil support links decrease with current as shown in Fig. 3, due to expansion of the coil in response to the magnetic hoop stress. The currents in the two

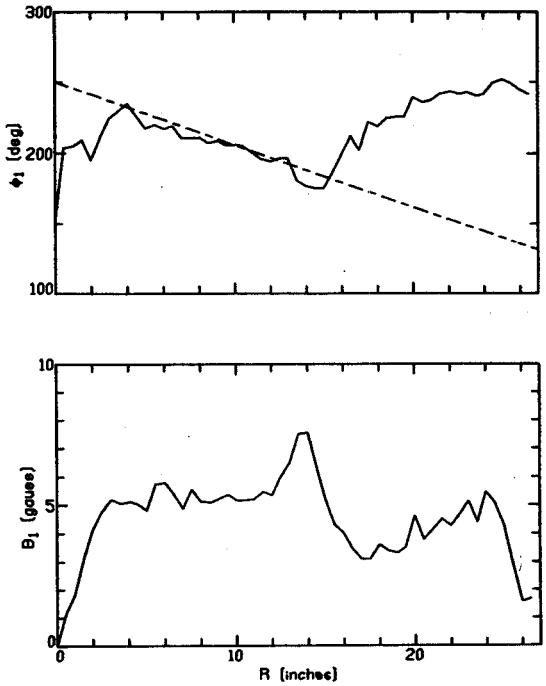


Fig. 2. Radial profile of phase ($\phi_1$) and amplitude ($B_1$) of first harmonic after convergence of the centering procedure. The slope of the dashed line represents the design spiral of the pole tips.

sections of the coil are equal for these measurements. The inequality of the three link forces at zero current is presumably due to forces exerted by refrigeration and instrument piping to the coil, friction in the coil support structures, and to errors in calibration of the gauge zero point. These zero current discrepancies are ignored. The sum of the magnetic (i.e. current-dependent) forces in the 3 links is calculated and divided by an experimentally measured coefficient to relate the net force to the centering error. These coefficients, (K), which are current dependent, and the displacement required to center the coil (magnitude d, direction $\phi_c$) are shown in Table I. These values may be compared with a displacement of 1.9 mils at 46° inferred from the first harmonic analysis which fits the measured harmonic from R = 25 inches to 26.5 inches.

The magnetic force K varies exponentially with current. It doubles in size for each increase in the current of 110 A ($I_S = I_L$).

Table I. Coil centering error inferred from link forces.

| I (A) | 400 | 500 | 600 | 700 |
|---|---|---|---|---|
| K (lbs/mil) | 34 | 65 | 117 | 214 |
| d (mil) | 5.3 | 3.9 | 2.8 | 1.7 |
| $\phi_c$ (deg) | 257 | 256 | 260 | 275 |

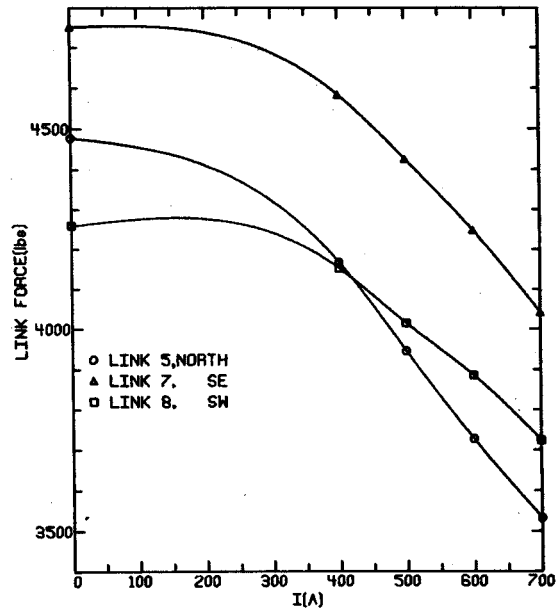


Fig. 3. Total force registered in each of the radial links vs. current in both main coils.

## 3. Tank Centering and Distortion-Mechanical Measurements

The shape of the cryostat inner wall in the midplane was measured before the first map by means of a dial indicator pivoted about the magnet center. The first and second harmonics in the field map were converted to mils of deviation from a centered circle using the value of the tank form factor at R = 26 inches (1.6 gauss/mil). The result is the curve shown in Fig. 4. The mechanical measurements are plotted as points on the same graph for comparison. An arbitrary constant has been added to the harmonic data to obtain the fit shown, since the indicator reference radius is arbitrary.

The analytical form of the function graphed as a solid curve in Fig. 4. is

$$\Delta r[\text{mils}] = 19 \cos(\theta-190) + 14 \cos [2(\theta-45)] + 15.6$$

Fourier analysis of the mechanical measurements gives

$$\Delta r[\text{mils}] = 20.5 \cos(\theta-201.5) + 12.2 \cos [2(\theta-51.9)] + 27.1 .$$

Harmonics higher than the second have amplitudes less than 1 mil and are neglected. The mechanical measurements of the cryostat evidently agree with the magnetic measurements at this stage, showing a centering error of 20 mils.

After MAP 30 was completed the radius gauge was installed in the magnet and the cryostat shape was measured again. These data and the shape inferred from the harmonics in the MAP 30 field are plotted in Fig. 5. The solid curve (magnetic measurements) is the function:

$$\Delta r = 1.8 \cos(\theta - 68.8) + 7.5 \cos [2(\theta-75)] + 20.3$$

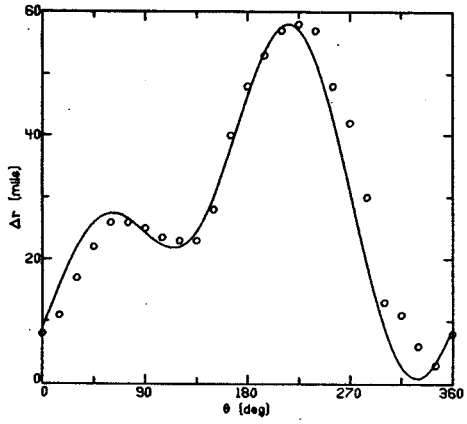


Fig. 4. Comparison of the locus of the cryostat inner wall as measured mechanically (circles) and inferred from first and second harmonics in the first map (solid curve). The only adjustable parameter in this comparison is a vertical translation, corresponding to the arbitrary reference for the mechanical measurements.

Fourier analysis of the mechanical measurements gives:

$$\Delta r = 7.5 \cos(\theta + 52.7) + 12.0 \cos [2(\theta - 56.4)] + 20.3$$

The mechanical measurements show that the tank is off center by 7.5 mils. The first harmonic in the field is equivalent to only 2 mils. Evidently there is another source of first harmonic (e.g. sector bars) which has been compensated by the tank offset. The field harmonics from this source have been deduced (see figure caption) by assuming the validity of the analysis procedure outlined above.

## 4. Azimuthal Angle Reference

The angular coordinate used for mapping the field and for all the present analysis is the same as the machine coordinate system but with rotated reference position. The origin for the mapping angle coordinate is at $+34.74^{\circ}$ in the machine coordinate system. The positive direction is counter clockwise, as seen from above. The approximate locations of the coil support links in the mapping coordinate system are given in Table II.

Table II. Link locations.

| | θ [deg] |
|---|---|
| North, link 5 | 60 |
| Southwest, link 8 | 180 |
| Southeast, link 7 | 300 |

## 5. Flip Coil Bar Centering Check

The flip coil bar is designed to operate with coil No. 2 over the axis of rotation (r = 0).

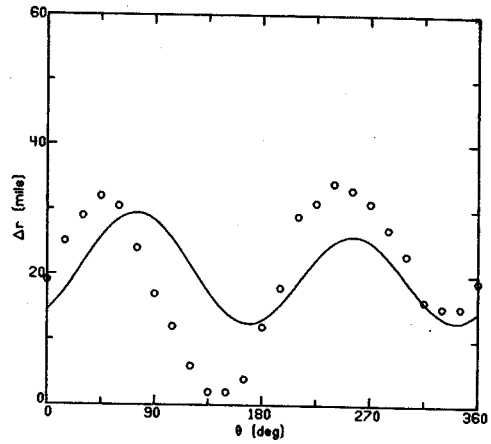


Fig. 5. Similar to Fig. 4 except measurements were done after the completion of the present centering program. The clear discrepancy between the two functions on the graph means that there is another structure besides the tank wall contributing to the first and second harmonics. By Fourier analysis of the difference between the mechanical and magnetic measurements of Δr shown, one finds that this structure produces (at r = 26 inches) a first harmonic of 5.4 gauss amplitude peaked at $\theta = 117^{\circ}$ and a second harmonic of 4.7 gauss amplitude at $\theta = 52^{\circ}$.

Coils 3 to 55 are spaced at 0.5 inch intervals to r = 26.5 inches. Coil No. 1 is located at r = -3 inches, so it ideally should measure the same field as coil No. 8 when the azimuth is increased by $180^{\circ}$. By comparing the amplitudes of the third harmonic measured by these two coils, we find that the center line connecting the coils is off the rotation axis by 11.5 ± .3 mils. This is inferred from the average difference in harmonic amplitude in 4 maps (13.75 ± .33 gauss) and the derivative $dB_3/dr$ = 1.2 gauss/mil at r = 3 inches. These measurements were done with the small coil excited to 600 A and the large coil at 448.2 A.

Based on mechanical tolerances, the estimated uncertainty in the locations of the coils with respect to the bar is ± 5 mils. The bar itself is centered with estimated uncertainty of ± 10 mils.

## 6. Summary

The coil and cryostat have been centered using the double criteria of minimum first harmonic and balanced link force. A residual centering error of the cryostat has been measured mechanically. Subsequent measurements of the locations of the sector bars show that an alignment error exists, which will require disassembly of the pole tips to correct it. This will be done, together with other machining and drilling operations on the iron scheduled for summer 1979. After reassembly the centering procedures will be repeated.

# Superconducting Magnet Cryogenic Operation

M.L. Mallory, H. Laumer and D. Poe

In previous annual reports, details of operating the superconducting magnet cryogenic system have been reported. During the past year, we have gained additional experience and have made many measurements; the results are reported below.

## Cryostat Liquid Helium Boil Off Measurements

Figure 1 is a measurement of liquid helium height in the top and lower sections of the superconducting magnet cryostat as a function of time. From the known volume of liquid helium one can calculate the liquid helium boil off rate. The boil off rate when the He level is at the top of the cryostat is the most relavent, since this denotes the minimum energy to be removed by the liquid helium refrigerator to keep the cryostat full of liquid helium. This rate is ~15 l/hr, which is ~2 times larger than calculated. The temperature of the liquid nitrogen (LN) shield at the lead port, (the most distant point from the LN containers that are in contact with the shield) is at 150 K. This warm LN shield can theoretically account for the increased heat load. The average boil off rate for allowing all the liquid helium to boil from the cryostat, the value previously reported, is ~9 l/hr.

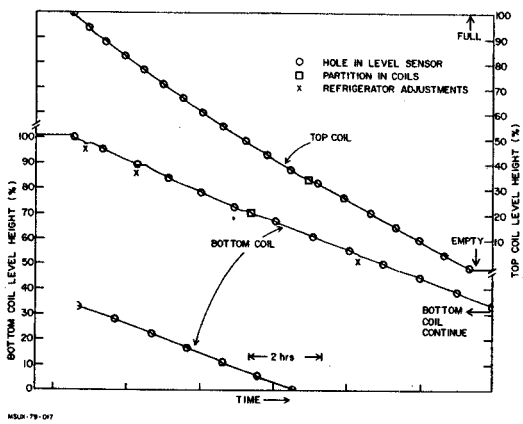


Fig. 1. The boil off curve for the superconducting magnet. The rate at the top of the cryostat is ~15 l/hr. The average boil off rate is ~9 l/hr. The fine structures due to holes in the level sensors are circled and the partition between the coils are boxed. This boil off rate curve was exactly the same after 5 months of operation.

The boil off data, shown in figure 1, has some interesting fine structure. This structure has been correlated with small holes that are drilled into the level sensor at 1" intervals. Two additional fine structure peaks were detected and are correlated with the partitions between the small and large coil. Level sensors also show transients when pressure changes, occasioned by adjusting refrigerator valving, occur. A liquid helium meniscus inside the level sensor is hypothesized as causing this fine structure.

## Direct Coupling of Refrigerator to Cryostat

In the normal operating mode, the refrigerator makes liquid helium into a 500 l dewar, and then the liquid helium is transferred to the cryostat. After a period of several months operation, an increased demand was detected upon the refrigeration capacity, or a decrease in the refrigerator output. A boil off measurement indicated that the cryostat heat load was unchanged. (A boil off measurement made 5 months after initial cooldown also showed the same boil off rate, thereby attesting to the long term constance of the cryostat heat load.) A warmup and decontamination of the refrigerator did not increase its output. Finally the vacuum jacket of the 500 l dewar was examined and found to have a high helium content. It is now realized that the 500 l dewar vacuum jacket must be pumped out on an annual maintenance cycle.

During the maintenance of the 500 l dewar, the refrigerator was connected directly to the cryostat and the refrigeration was successfully matched to the magnet boil off rate. No obvious change in total system heat load was detected in this mode of operation.

## Eddy Current Boil Off Detection

The direct coupling of the refrigerator led to the detection of eddy current heating in the coil and it is shown in figure 2. In figure 2, the helium level height of the lead port is shown as a function of time. The current from the superconducting magnet is also shown. The current from the power supply initially flows thru the dump resistor and then charges the coil. The peaks in the current data is a planned overshoot in order to quickly establish stable coil current. The magnet was charged from 200 to 300 and finally to 400 amps. On discharge, the coil current was dropped directly to zero current.

The superconducting wire in the magnet coil is banded by a multiturn layer of aluminum which provides support to the superconducting wire. This aluminum bonding acts like a one turn transformer and a change in magnetic flux thru it produces an eddy current flow which then boils liquid helium. The boiled liquid helium forms gas bubbles in the bath which cause the helium level to rise. The height increase is seen in figure 2 for charging the magnet and from this increase an estimate of the helium boiled can be made and the energy calculated. This energy compares favorably with that predicted from the eddy current calculation thru the banding. After the heating stops, the bubbles migrate to the top of the helium bath

and the liquid level height drops. This migration time appears to be on the order of minutes for our cryostat.

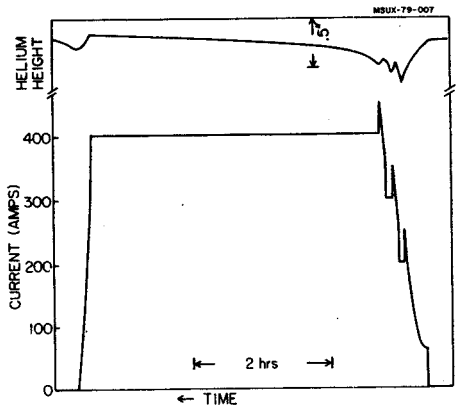


Fig. 2. The level sensor response in the lead port and the power supply current as a function of time. The level sensor height variations are due to eddy currents in the magnet coil banding.

Figure 2 also shows that the eddy current heating is different from charging and discharging the magnet. Magnetic field measurements show that in charging the magnet, the magnet iron is aligned as the current initially increases until it is saturated. In discharging, the magnetic field due to the iron is not changed by the current as much, since the current does not go negative, hence the demagnetization time of the iron comes into consideration and it appears to be in the 10's of minute range. The increased helium height is seen simultaneously in all ports and thereby eliminates a proposed splashing phenomena. When transferring liquid helium from the 500 l dewar, the change in helium height due to eddy current heating is much reduced. The eddy current heating is also believed to produce a pressure increase in the cryostat. For instance, when the magnet is dumped (removal of all current in ~3 minutes) from the maximum current, a large pressure pulse is detected. This increase in pressure would stop the liquid helium transfer from the dewar, whereas such a small pressure change would have minimal effect upon the liquid helium quantity supplied directly from the refrigerator.

Helium Leak Results

Helium leaks from the coil bobbin into the cryostat vacuum jacket have been detected and a leak in the refrigeration port of the cryostat was localized by the cold gas technique reported previously. The exact location of the leak was traced to a weld that was made on the inside of the coil bobbin. The outside of the bobbin showed only slight heat marks and this area had not been leak tested. Finding this leak has led to the realization that these internal welds must also be vacuum tight and done carefully. The leak location was below the exit of the top fill liquid helium line of the cryostat and with it repaired, it was discovered that liquid helium completely filled the refrigeration port. Secondly the top fill liquid helium line was used successfully to completely fill the cryostat with liquid helium. We confirmed our hypothesis that the coil is completely cooled before any liquid accumulates, whereas the bottom fill liquid helium line allows liquid accumulation even while the top port of the cryostat is warm (20 K)

Heat Pulse Observations

Heat pulses (the introduction of heat energy into a cold cryostat) must always be taken into account, when making changes in the refrigerator valving or in transferring liquid helium. Observation of these heat pulses over the past year and coupled with pressure and temperature measurements has led to a better understanding of what is occuring. Experiments on the 500 l dewar with a temperature probe showed that as a warm transfer line is cooled, the warm gas flows into the top of the dewar and the gas does not sink down to the liquid helium surface but stays near the top and is returned to the refrigerator, with only a small increase in pressure. The transfer line cools until at a temperature slightly below 20 K, a large increase in the pressure is observed. The refrigerator gauges indicate that liquid helium is being produced at the JT valve and two phase helium is being transferred to the dewar. It is proposed that the two phase gas is transferred to the top of the dewar, where the liquid drops then try to fall to the liquid surface. As the drops fall, the helium is boiled and a turbulent gas flow condition occurs. It then becomes possible for the 20 K helium gas to come in contact with the liquid helium surface resulting in a large boil off and the observed pressure increase.

The same phenomena is also sensed when introducing liquid helium to the top of the magnet cryostat. In this case we are able to measure the gas return temperature and the pressure in the top of the cryostat. Initially the gas return temperature can go as high as 150 K, with only a slight pressure increase. As the temperature drops below 30 K, the pressure in the cryostat surges from 3 psi up to 6 psi. This pressure would surge higher but the transfer rate is usually limited. Finally, when the return temperature approaches 7 K, the pressure in the magnet cryostat drops to 3 psi and liquid helium accumulates. Again this pressure surge is very suggestive of occuring when two phase helium is transferred.

Measurement of a Transfer Line Heat Load

The total heat load of the refrigerator is composed of both the magnet cryostat and the transfer lines. An experimental method of measuring

the heat load of a transfer line was detected during the cooldown of the coil. The coil temperature was at ~20 K and at this temperature the sensor indicates that it is at a uniform temperature. The cooldown of the coil was stopped and the refrigerator put to making liquid helium into the 500 l dewar for ~4 hrs, while the transfer line to the magnet was allowed to gradually warm up. The refrigerator was then revalved to the magnet coil and the temperature response of the coil is shown in figure 3. Assuming the coil is acting like a calorimeter, we are able to calculate the heat pulse energy. The time that the transfer line warmed, allows calculation of its heat load. Although this technique may have large errors and we did not sysmatically reproduce the results, the value obtained was near that calculated for the transfer line.

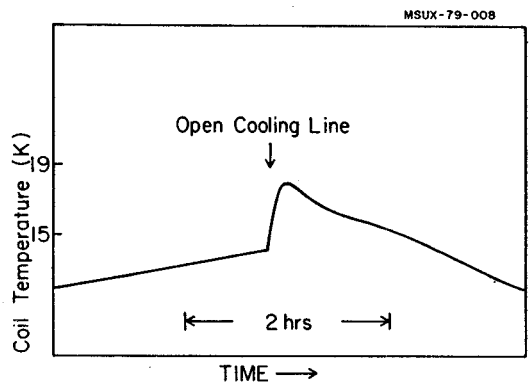


Fig. 3. The temperature response of the superconducting coil when hot gas from a transfer line is put into the coil. The heat pulse allows an estimate of the transfer line heat load; it was found to be near the calculated value.

Liquid Helium Level Operations at the Top of the Cryostat

As the internal helium leaks into the cryostat vacuum jacket have been repaired, the helium level height in the three top ports have responded differently. The refigerator port is connected with vent lines to the safety port and the lead port. The exits of these vent lines are above the top of the level sensors in all ports. The vent line passes thru the cryostat reservoir and is under liquid helium when the reservoir is full. After the reservoir is full, liquid helium enters each port and the boil off gas in each port is returned to the cold gas return of the refrigerator thru the internal vent line or thru exterior helium vent lines which are at room temperature. Fixing the helium leak has resulted in the refrigerator port liquid level always being above the top of its level sensor.

In the lead port, the liquid level initially goes to 60% height and stabilize, with the gas flow thru the room temperature vent line at 6000 cc/min. This flow is approximately a factor of three less than the calculated boil off rate due to the current leads and the remaining boil off gas is assumed to be returning via of the internal vent line. If the room temperature gas flow is increased beyond 10,000 cc/min., the liquid helium height increases beyond the top of the level sensor. Shortly there-after the helium level rapidly drops and finally stabilizes at the top of the helium reservoir. Varying the external flow does not change the level height. It is hypothesised that the internal vent line is filled with liquid helium, when the level height increased beyond the top of the level sensor, with the consequence that no boil off gas can return via this line and now the boil off gas can return only via the top of the cryostat reservoir. If the liquid helium is allowed to boil out of the cryostat reservoir, thereby allowing the helium in the vent line to boil, the level height in the lead port will again stabilize at the 60% value at refilling. We conclude from these observations that the liquid level in the refrigerator port is not above the top of the lead-refrigerator vent line exit.

The operations of the safety port level sensor has also change with the fixing of the helium leak. Namely, the liquid level is now at the top of the cryostat reservoir, whereas in the past it has had liquid in the port. Increasing the flow in the external line does allow liquid helium to enter the port. This data is very suggestive that the vent line between the safety-refrigerator ports is normally full of liquid helium and the boil off gas returns via the top of the cryostat reservoir when the external line flow is restricted.

Cryogenic Failures

During the past year, we have experienced some failures of the cryogenics system. In general they have been quickly repaired and operations continued. Failures of both the diffusion pump and mechanical pump on the helium cryostat vacuum jacket have occurred and in each failure, only minor effects upon the cryogenic system occurred.

The early detection of failure problems and immediate action for repairs leads to small down time. The cryogenic system is a closed loop and usually any problem shows up rapidly on the pressure of the return gas line. A sensor has been constructed that detects any pressure surges on the return gas lines that cause the low pressure pop off to be open. This constant monitoring alarm has greatly increased the cryogenic system reliability.

In summary, we have surprisingly detected many interesting operational results during the past year and it is hoped that the detail description of these results will be beneficial to future superconducting cyclotrons.

# Study of Vertical Motion in the Central Region of the K = 500 MeV Cyclotron

M.M. Gordon and E. Liukkonen

Last year's Annual Report contained a description of the new Cyclone program which is designed to calculate particle orbits in the central region of the cyclotron. Since the electric field plays a crucial role in this region, the calculations are based on realistic fields derived from detailed measurements using an electrolytic tank.

Since last year's report, the Cyclone program has been extended to include the calculation of vertical motion. As far as we know, such calculations have never been carried out before except through the use of crude models.

The crucial design goal here is to avoid electric defocusing of the orbits during the first few turns just beyond the source-puller. The usual simple model of the process provides a useful guide, but only a qualitative one. For example, with our $60^{\circ}$ dees operating on harmonic h = 1, we expect the ions to be focused on entering a dee and defocused on exiting, since the voltage is falling in the former case and rising in the latter. As a general rule, the net effect will be focusing if the particles arrive "late", that is, have positive phase.

For our central region geometry, this simple rule is difficult to apply where electric focusing is most likely to be important, namely, just beyond the puller. Here, the particles exit dee #1 and enter dee #2 in a region where the electrode structure has been considerably deformed in order to improve the energy gain. The problem of evaluating electric focusing in this region and on the remainder of the first turn provided the main incentive for extending the Cyclone program.

The electrolytic tank measurements yield values of the individual dee potentials in the median plane, and these values are superimposed with appropriate time factors to produce the resultant potential V(x,y,t). As long as motion is restricted to the median plane, only first derivatives of this potential are required. However, in order to include vertical motion, one needs second derivatives at least.

The need for second derivatives usually poses serious problems since their calculation will not be physically meaningful unless the potential measurements are sufficiently accurate. During recent years, the accuracy and smoothness of the potential data have improved sufficiently to make feasible the calculation of vertical motion with reasonable success.

Except where electrodes are present, the electric field satisfies the condition: div . $\vec{E} = 0$. Assuming, in addition, that the electric potential is symmetric about the median plane, we then obtain: $E_z = z(LV(x,y,t))$, where L denotes the two-dimensional (x,y) Laplacian operator. This expression for the vertical component of the electric field is correct to first order in z and, as expected, involves the second derivatives of V.

The measured potentials are stored in a square lattice having a uniform 0.04 inch spacing in both directions. A straightforward interpolation-derivative procedure is used to obtain values of the Laplacian, along with values of the potential and its first derivatives, as they are needed in the program. Difficulties arise only when the orbit comes too close to one of the electrodes penetrating the median plane, where the second derivatives become meaningless due to the discontinuity of the electric field. Therefore, a special provision has been made to handle this situation. If the orbit is closer than three grid-unit lengths to any electrode, a straightforward two-point extrapolation process is initiated, where the radius is successively increased by one grid-unit length. The potentials, first derivatives and Laplacians are calculated at these two points. Finally a line is placed through these points back to the original radius. This simple extrapolation procedure removed adequately all abnormalities in the vicinity of the electrodes.

The axial motion in the central region of the K = 500 MeV cyclotron was studied using an earlier electrolytic tank model ("version 4") which gave adequate overall clearances in the first harmonic operation of the cyclotron, but which was seriously restricted only for the high-turn-number cases ($540 \pm \frac{20}{50}$ revolutions). (The present version is labeled as "version 8", and it is described in a separate contribution in this progress report.)

Figure 1 shows the median plane electric field of the version 4 central region as an equipotential contour map, together with the central-ray orbits for our model particles with q/m = 0.322 (e.g., $^{28}Si^{9+}$) which will be accelerated to 52 MeV/A final energy.

Figure 2 shows the z and $p_z$ values along the central-ray orbits of Fig. 1 as a function of turn number. The z variation is a smoothly oscillating curve from which the axial focusing frequency can be simply extracted for each quarter wave length. The $p_z$ oscillation has the same frequency as the z variation, and it shows more clearly the superimposed rapid oscillations associated with the dee structure. (Since the representation of the axial motion in the program is strictly linear, no scales are shown for z and $p_z$, but one can imagine the scales to be in inches.) The starting conditions in Fig. 2 were z = 0 and $p_z = 0.025$.

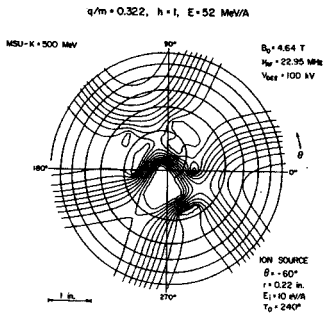


Fig. 1. An equipotential contour map of the h = 1 central region which was used in studying the axial focusing in the center of the K = 500 MeV superconducting cyclotron. Also shown is the central-ray orbit for the q/m = 0.322 particles ($^{28}Si^{9+}$) which served as a "model particle" in this study.

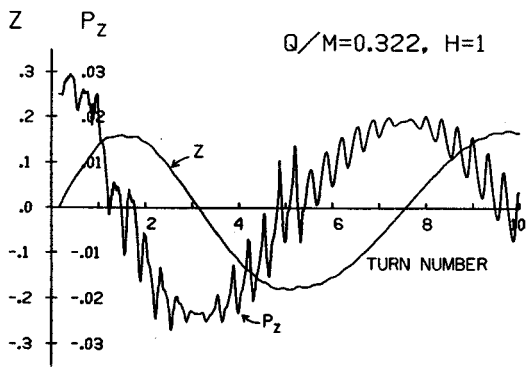


Fig. 2. z- and $p_z$-motions of the q/m = 0.322 (h = 1) particles for the first ten revolutions along the central ray of Fig. 1. The transition from the measured electric field to the region where the energy was incremented only in gap crossings ($r \geq 2.8$ inches) occurs during the fifth revolution, as clearly seen in the figure.

From the linear representation of the axial motion it follows that one needs only another ray with the starting values, e.g., z = 0.1 and $p_z$ = 0.0, and all the other rays can be calculated using the transfer matrix method. This method was used in studying the axial phase-space behavior. The results are represented in Fig. 3, which shows the behavior of an ellipse, starting upright in the z = 0.1 and $p_z$ = 0.025 as major axes, during the first five revolutions along the central-ray orbit of Fig. 1. As can be seen in Fig. 3, the behavior of this ellipse is smooth. The axial dimension of the beam increases about a factor of two during the first five turns.

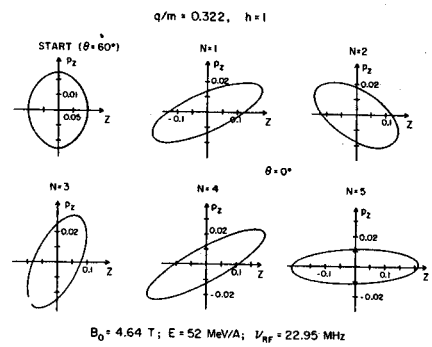


Fig. 3. The behavior of an ellipse, which starts upright with z = 0.1 and $p_z$ = 0.025 as major axes, is followed for the first five revolutions in $z,p_z$-space. The ellipses are plotted once per revolution at θ = 0.

The strength of the axial focusing is known to decrease rapidly when the speed of the particles increases. As mentioned earlier, more positive phase values should give more axial focusing. These findings are well-confirmed also in this case. This can be seen in Fig. 4, which displays the axial-focusing frequency $\nu_z$ as a function of radius for four different starting times $\tau_o$. (Here the starting time, e.g., $\tau_o = 240^o$, means that the particles leave the ion source $30^o$ before the negative peak RF voltage.) The lowest curve in Fig. 4, denoted by the "$\nu_z$ cone", represents the magnetic axial focusing which in the K = 500 MeV SCC is produced by a magnetic hump placed into the center of the cyclotron. (The shape of the magnetic hump or cone is in our case created purely mathematically by requiring $\nu_z$ = 0.1 for r < 5 in.) The height of the $\nu_z$ curve above the magnetic values represents the axial electric focusing. As can be seen in Fig. 4, the axial electric focusing is stronger for the later starting times (i.e., more positive phase). The focusing is very strong ($\nu_z$ = 0.3 for $\tau_o = 240^o$) when the particles enter the first acceleration gap ($r \leq 1$ in.), but it falls rapidly with radius when the radius of the particle increases. At a radius of three inches there is practically no axial electric focusing left, but soon after this radius the sectors begin to produce focusing.

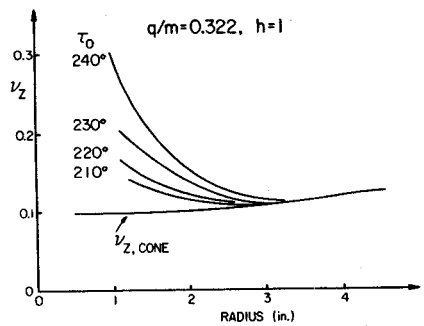


Fig. 4. Axial focusing frequency $V_z$ as a function of radius for four different starting times of ions from the ion source. Details are explained in the text.

# Calibration of Magnet Mapping Apparatus

P. Miller, G. Bellomo, B. Jeltema, H. Laumer, D. Poe, F. Resmini, G. Stork

The magnetic field mapping probe contains 55 flip coils spaced along a radial bar, each connected to its own integrator for readout of the magnetic field. The change in the integrator output voltage ($\Delta V$) that occurs when the bar is flipped is assumed to be proportional to the magnetic field (B) at the flip coil center:

$$B = k\,\Delta V \qquad (1)$$

The calibration constant is determined for each integrator by installing the probe in a 46 inch diameter magnet with a 6 inch gap. (see Fig. 1).

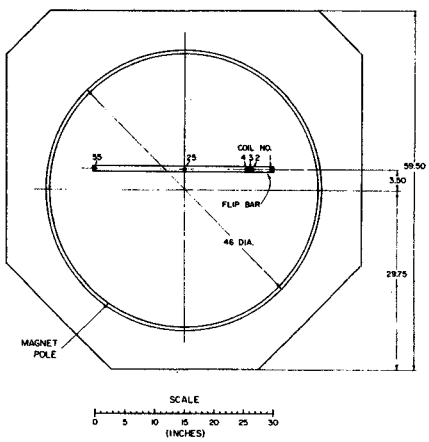


Fig. 1. Top view of the calibration magnet chamber showing the location of the flip bar containing the 55 coils.

The magnet produces uniform field of about 12 kgauss. The magnetic field is measured precisely at intervals of 2.5 inches along the top surface of the bar with a proton nuclear magnetic resonance probe before and after a calibration run. The probe is inserted through the open side of the vacuum tank, at the top of Fig. 1. A sample of these data are shown in Fig. 2.

The field is interpolated linearly between measurements as shown. This leads to an error of less than 25 ppm. Saturation of the edges of the pole tips rapidly makes the field become less uniform as the magnet current is raised above the value that gives the field pictured in Fig. 2. The 12 kgauss level is the highest that is practical for calibration of all coils at once.

The bar flipping mechanism and the operations for reading and recording the integrator output voltage are controlled by a PDP 11/20 computer containing the program used for mapping the magnet. The voltmeter (Hewlett Pachard HP3490 A) is connected to each integrator in turn via a relay multiplex switch (Matrix Corp. 1701) under control of the computer. The calibration constant k is inferred from eqn (1) by off-line analysis. A file containing these constants is supplied to the original program when it is used for mapping, so the output record is in magnetic field units.

Temperature corrections are not applied at this stage, but are done off-line after the original data are copied into the files of the Sigma-7 computer.

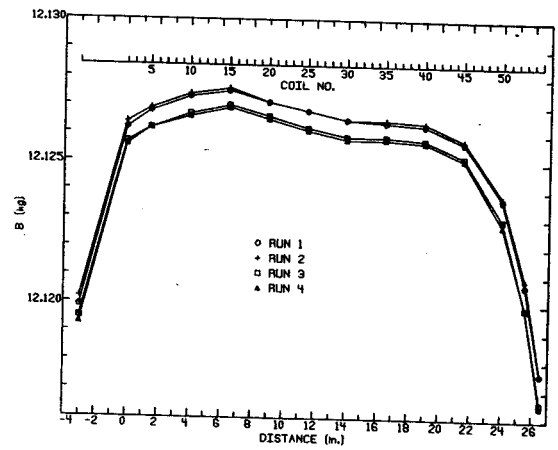


Fig. 2. Distribution of magnetic field along the flip bar in the calibration magnet. Note the suppressed zero on the ordinate. The points represent measurements with a nuclear magnetic resonance probe at intervals of about 2.5 inches.

Table 1 gives a list of contributions to the uncertainty in a single measurement of k with the estimated magnitude of the uncertainty from each source. Where a range is given it reflects the variation of the estimate among the 55 coils or integrators.

The first two items refer to the effect of positioning inaccuracy of the NMR probe. The axial position is determined by the thickness of the flip bar and the probe. In future work this term will be eliminated by applying a correction calculated from the field derivatives. The horizontal term is due to uncertainty in the location of the sensitive region in the probe (since remedied by an X-ray photo) and to poor visibility inside the magnet. Both estimates depend on field derivatives which vary considerably along the array of coils. An estimate of the reproducibility of the NMR field measurements can be gained from Fig. 3.

The frequency counter accuracy is not an important issue, since all 55 channels are affected equally by any error in its calibration. Relative errors between channels are more important for Cyclotron design purposes.

Line 5 represents the lack of reproducibility of repeated measurements in the calibration magnet. This uncertainty is attributed to noise and non-

The temperature difference for the flip coils were produced by temperature changes of the calibration magnet itself. The magnet poles gradually warm up for about 2 days when the magnet is on. This temperature change (up to 3°C) is transmitted to the flip coils inside the gap. A thermal enclosure with temperature regulation will be used in future calibrations to reduce the uncertainty in coil temperature and to insure greater uniformity of temperature along the array of flip coils.

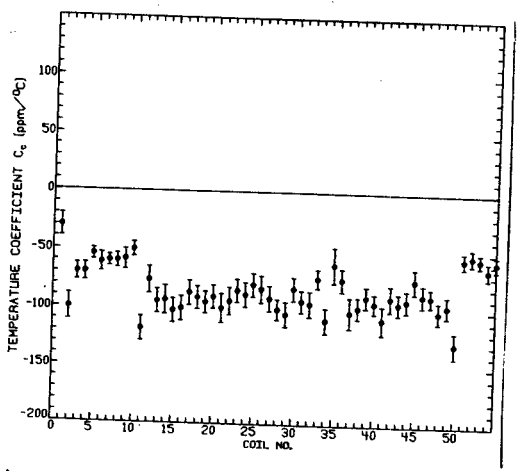


Fig. 6. Measured temperature coefficient for each flip coil ($C_c$).

# Z-Probe Design

H. Laumer

A probe which senses the azimuthal position of the beam in the cyclotron is essential as a beam diagnostic tool. A Z-probe made up of a number of identical current sensing elements (called fingers hereafter) is considered. Evidently a design with the minimum number of fingers which still adequately sense Z-oscillations is most economical.

To determine a design criterion for the fingers, the beam is assumed to be uniform in intensity and rectangular in cross section. Finding the center of the beam distribution is then sufficient to characterize a Z-oscillation. Fig. 1 summarizes probe and beam geometry parameters for this simple model. It is assumed a beam of azimuthal dimension h is completely intercepted by a probe made up of fingers which have a vertical dimension D. The parameter W in Fig. 1 represents the overlap between the beam spot and one of the extreme fingers struck by the beam.

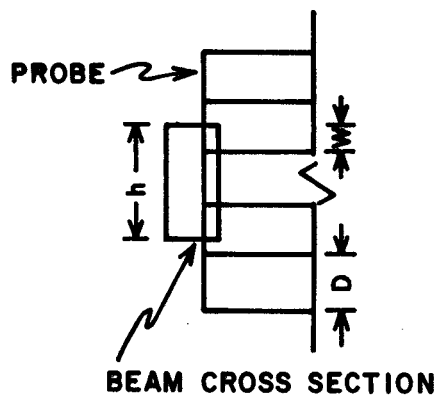


Fig. 1. Overlap schematic between beam and five-fingered probe. h = beam spot height; D = vertical dimensions of a finger.

The error with which the center of the beam distribution is determined is given by the equation:

1) $\frac{D^2}{2h}\left[\text{frac}\left(\frac{h}{D}\right) - \frac{2W}{D} - \left[\text{frac}\left(\frac{h}{D}\right)\right]^2 + \frac{2W}{D}\,\text{frac}\left(\frac{h}{D}\right)\right]$

for $\frac{W}{D} \leq \text{frac}\left(\frac{h}{D}\right)$

2) $\frac{D^2}{2h}\left[-\text{frac}\left(\frac{h}{D}\right) - \left[\text{frac}\left(\frac{h}{D}\right)\right]^2 + \frac{2W}{D}\,\text{frac}\left(\frac{h}{D}\right)\right]$

for $\frac{W}{D} > \text{frac}\left(\frac{h}{D}\right)$

where A = int (A) + frac (A) and int. (A) is an integer and frac (A) < 1. There are always values of W for which the error is 0, but no design can take advantage of this fact.

The magnitude of the maximum error possible, given h and D, is then equal to:

3) $\left[\text{frac}\left(\frac{h}{D}\right) - \text{frac}\left(\frac{h}{D}\right)^2\right]\frac{D^2}{2h}$

It is evident that for $\frac{h}{D}$ = integer the error is always 0. Hence a beam probe design with finger dimension D equal to the expected average beam dimension h is optimum. The maxima of eq. (3) are found to be at:

4) $h = D\sqrt{N^2+N}$ where $N = \text{int}\,\frac{h}{D}$,

with maximum error $= D\left\{\frac{1+2N}{2} - \sqrt{N^2+N}\right\}$

Hence, if it is possible, the finger size D is to be chosen so h is a multiple of D and the values $D = \frac{h}{\sqrt{N^2+N}}$ are to be avoided. From Table 1 it is apparent that little is gained by making D much smaller than the expected beam spot size h.

Table 1.

| | Beam spot size (multiples of D) | Maximum possible error (multiples of D) |
|---|---|---|
| An Optimum | 0 | 0.5 |
| | N (any integer) | 0.0 |
| Dimensions to be avoided | $\sqrt{2}$ | 0.086 |
| | $\sqrt{6}$ | 0.050 |
| | $\sqrt{12}$ | 0.036 |

It is also probably a good idea to pick an odd number of fingers since then no insulating gap falls at the equilibrium Z plane which might leave beam unintercepted.

A computer model simulation of a multiple finger probe design was also programmed. The finger geometry included a) open gaps between fingers for insulation, and b) recessed fingers to presumably capture secondary electrons. The program proceeds by assuming a uniform rectangular beam distribution. This distribution is divided up into cells, an array (IZ, IR), and the fate of individual cells is followed until eventually a probe finger is struck.

The location of the beam spot along the radial axis is assumed to be given by the equation: $R = Ro\sqrt{N}$. The width of the beam spot in the radial direction is assumed to be constant.

The azimuthal position of the beam spot is given by:

$$B + A\cos(2\pi\nu_Z N + TH)$$

$\nu_Z$ is the Z oscillation frequency (# of cycles/# of turns), N = turn number, TH = an adjustable

phase angle, A gives the magnitude of the Z oscillation. The vertical size of the beam spot is programmed to be the projection of an ellipse, rotating in Z phase space, onto the Z axis. The program can then test the response sensitivity of the probe to variations:

a) Probe geometry: 1) finger spacing
2) recess-cut radius

b) Beam geometry: 1) phase angle
2) Z oscillation amplitude
3) radial beam spot size
4) azimuthal beam spot size

Output from the program are the following:

1) A printer plot of the beam intercepted by each finger as a function of radial probe position.

2) A printer plot of the center of the beam distribution as a function of Z and R as calculated from the beam intercepted by the probe fingers. For comparison the function A cos $(2\pi\nu_z N + TH)$ is also plotted on the same axis.

3) Finally, a sine curve is fitted to the probe data to obtain the amplitude of the Z-oscillation as detected by the probe. This can then be compared to the input data $Z = A \cos (2\pi\nu_z N + TH)$.

This comparison is not quite justified. The expected response for a beam which is very narrow in the radial direction is a histogram type graph (Fig. 2).

However, to extract Z oscillation information from data taken with a real Z probe, fitting with a sign curve is a simple expedient.

The summary in Table 2 gives some idea of the probe performance and is based on analysis from fitting a sine wave to the Z probe response.

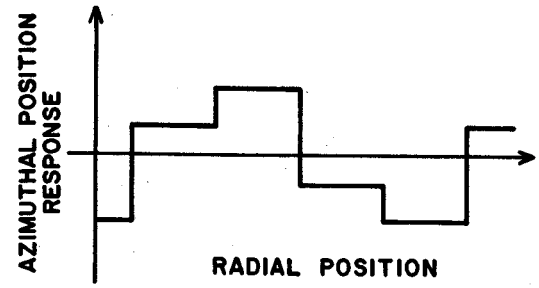


Fig. 2. Probe response for a Z oscillation of a beam with narrow radial cross section.

In the table are listed the unaccounted phase shift and the amplitude ratio between the sine wave fit and the input Z oscillation. The majority of the cases listed assume a five finger probe with a gap area equal to 10% of the total area covered by the probe. Special cases representing wider gaps or three finger probes are noted in the comments column. The column marked "finger shape" identifies the two geometries tested. There R stands for a recessed finger with a concave radius equal to 1/2 the finger width, and ST stands for a straight edged finger. The column marked "spot size" gives the range of the azimuthal extent of the beam. Radially the beam was assumed to be 0.06 inches wide for all cases. The largest discrepancies between the fit and the assumed Z-oscillation input parameters occur for small Z-oscillation and wide gaps between fingers, none of which is surprising. On the average the amplitude is determined to better than 15% and the phase is determined to better than 10°; this may be compared to the radial width of 0.06 inches for the beam spot which represents a phase angle of about 20°.

Table 2.

| Run # | Amplitude ratio | Beam spot phase angle (TH) | Phase error of fit in degrees | Z-oscillation amplitude in inches | Spot size in inches | | Finger shape | Comments |
|---|---|---|---|---|---|---|---|---|
| | | | | | Max | Min | | |
| 5 | 1.24 | 0 | 4.9 | 0.05 | 0.2 | 0 | R | |
| 6 | 0.89 | 0 | - 4.7 | 0.3 | 0.2 | 0 | ST | |
| 7 | 1.07 | 0 | - 4.7 | 0.17 | 0.35 | 0 | ST | |
| 9 | 0.71 | 0 | 1.6 | 0.05 | 0.2 | 0 | ST | 50% gap width |
| 10 | 0.48 | 0 | 1.0 | 0.3 | 0.2 | 0 | ST | 50% gap width |
| 22 | 0.04 | 0 | 15 | 0.17 | 0.4 | 0.2 | ST | |
| 18 | 0.99 | 18 | 20.2 | 0.3 | 0.19 | 0.06 | ST | |
| 19 | 1.19 | 18 | 22.7 | 0.2 | 0.19 | 0.06 | ST | |
| 20 | 0.89 | 18 | 1.2 | 0.3 | 0.19 | 0.06 | R | 3 finger probe |
| 21 | 1.11 | 18 | - 0.3 | 0.2 | 0.19 | 0.06 | R | 3 finger probe |
| 23 | 0.04 | 18 | 7.0 | 0.17 | 0.4 | 0.2 | ST | |
| 12 | 1.13 | 36 | 14 | 0.05 | 0.16 | 0.12 | ST | |
| 15 | 1.1 | 36 | 0.9 | 0.05 | 0.16 | 0.12 | R | |
| 17 | 0.75 | 36 | - 9.0 | 0.25 | 0.16 | 0.12 | ST | |
| 11 | 0.83 | 45 | 44 | 0.05 | 0.14 | 0.14 | ST | |
| 14 | 0.83 | 45 | 6.6 | 0.05 | 0.14 | 0.14 | R | |
| 24 | 1.14 | 45 | 10 | 0.17 | 0.4 | 0.2 | ST | |
| 3 | 1.17 | 60 | 24 | 0.25 | 0.17 | 0.10 | R | |
| 4 | 1.17 | 60 | 5.6 | 0.25 | 0.17 | 0.10 | R | |
| 8 | 1.12 | 60 | 19 | 0.175 | 0.3 | 0.18 | ST | |
| 13 | 0.88 | 60 | -41 | 0.05 | 0.3 | 0.1 | R | |
| 25 | 1.10 | 60 | 0 | 0.17 | 0.4 | 0.2 | ST | |

# A Method for Calculating the Vacuum Requirements of Heavy Ion Cyclotrons

M.L. Mallory

## INTRODUCTION

In the late 1960's, a large number of isochronous cyclotrons successfully accelerated light heavy ions[1,2] and it was experimentally recognized that the vacuum systems, which were primarily designed for hydrogen and helium beams, were not adequate for large transmission of heavy ions.[3] At that time, a quantitative method for predicting the vacuum requirements for cyclotrons did not exist and therefore cyclotron builders tended to add as much pumping capacity to their cyclotrons as possible, that being more oil diffusion pumps located on the periphery of the acceleration chamber. The pumping due to this addition was minimal since the acceleration region between the pole tips was conductance limited by the narrow magnet gap and dee and a large fraction of the gas load is due to the ion source located in the magnet center. The pumping problem was solved by the development of thin cryopanels[4] that were mounted in the magnet gap and provided large pumping speeds at the right location.

At Michigan State University, a heavy ion superconducting cyclotron facility is under construction.[5] The desire to properly design the vacuum system for this accelerator has led to a reevaluation of past methods used to calculate vacuum requirements and the incorporation of the latest concepts into an analytical method.

## PREVIOUS HEAVY ION VACUUM CALCULATIONS

Most previous heavy ion vacuum calculations exist as accelerator design notes. The first realistic attempt at calculating the vacuum requirements of a heavy ion cyclotron that I have found was for the Variable Energy Cyclotron (VEC)[6] at Rutherford Laboratory and was done for the light heavy ions where some experimental cross section measurements existed.

In the Omnitron proposal,[7] the following transmission equation was used to establish its vacuum requirements:

$$n/n_o = \exp - (10^{10} P_{eff} t), \qquad (1)$$

where n is the number of ions accelerated to full energy, $P_{eff}$ is the effective or average pressure in the acceleration chamber (Torr) and t is the acceleration time (sec). In their derivation, it was assumed that $\sigma_L \beta = 10^{-17}$ cm$^2$/atom where $\sigma_L$ is the charge exchange loss cross section and $\beta = \frac{v}{c}$, where v is the ion velocity.

For the Darmstadt heavy ion linear accelerator (Unilac), Betz and Schmelzer[8] used a semi-empirical formula for the charge exchange cross sections and they are given below:

$$\sigma(q, q-1) = Aq^2 \left(\frac{v}{v_o}\right)^{-5}, \qquad (2)$$

where $\sigma(q,q-1)$ is the charge pickup cross section, q is the ion initial charge state, v is the ion velocity, $v_o$ is the Bohr velocity and A is an experimentally determined constant obtained from low energy sulfur data.

$$\sigma(q, q+1) = A\,(1+q)^2 \left(\frac{v}{v_o}\right)^{-5} e^{\frac{-2\,(q-\bar{q})+1}{\frac{\Gamma^2}{4}}} \qquad (3)$$

where $\sigma(q, q+1)$ is the charge stripping cross section, $\bar{q}$ is the mean charge state of an ion at a given velocity v and $\Gamma$ is the width of the charge state distribution. Empirical relationships for $\bar{q}$ and $\Gamma$ were determined from experimental data.

Finally the review article published by Betz[9] in 1972 contains the theoretical models for charge exchange cross sections and all of the then existing experimental data. Our initial attempts at calculating vacuum requirements were based on the above data and methods, but as additional theoretical understanding of charge exchange cross sections in various ion velocity regions have been published, we have reformulated our calculational method and it is presented in the following sections.

## CHARGE EXCHANGE CROSS SECTION

The attenuation of a beam of particles (dn) in traversing a distance dl in a vacuum chamber having $N_i$ atom/cm$^3$, where i denotes a specific background species, is the following:

$$dn = n \sum_i N_i \sum_m \sigma_i (q, q+m)\, dl, \qquad (4)$$

where q is the ion charge and m can be both positive and negative. In the acceleration process, $\sigma(q, q+m)$ is a function of velocity. At low velocity charge pickup processes occur and at high velocity charge stripping processes are dominant. The derived analytical expression used for these different cross sections as a function of velocity and mass follows.

### a. Pickup Cross Section

A large amount of experimental[10] and theoretical research has been done by atomic physicists interested in finding losses in thermonuclear plasmas. They have measured low energy charge pickup cross sections for highly stripped ions (typical of cyclotron ion source performance)

and have derived a theoretical model. (Previous accelerator vacuum models go to very large and unrealistic values at low energy, i.e. the energy of the first few turns in the cyclotron.) The theoretical model of Olsen and Salop[11] has been used to calculate the charge pickup cross sections ($\sigma_p$) at essentially zero energy for the cyclotron and is given below:

$$\sigma_p \ (E \simeq o) = \pi R_c^2 \qquad (5)$$

$$R_c^2 \ e^{\ 2.648 \times R_c/q^{1/2}} = 2.864 \times 10^{-4} \ q \ (q-1) v, \qquad (6)$$

where the ion incident velocity (v) is set equal to $7 \times 10^7$ cm/sec for masses < 150 amu.

$$\alpha = I_t / 13.6 \qquad (7)$$

where $I_t$ is the ionization voltage (ev) of the least bound electron of the target atom. All ionization potentials have been obtained from the calculation of Carlson.[12] Values for $R_c$ (the effective collision radius) are obtained by a numerical iterative routine. Another pickup cross section data point can be obtained from equilibrium charge state experimental data. Namely, Betz[13] has derived an empirical equation for relating the velocity at which the accelerated ion of charge q is in equilibrium with the charge pickup and charge stripping for single collisions.

$$v = v_o Z^{2/3} \left[ \ln \left( 1 - q\frac{h}{c} \right) \right] , \qquad (8)$$

where $v_o$ is the Bohr velocity ($2.19 \times 10^8$ cm/sec) and Z is the atomic number of the accelerated ion. At this velocity,

$$\sigma_p \ (E = \bar{q}) = \sigma_s \ (E = \bar{q}) \ . \qquad (9)$$

$\sigma_s$ is the stripping cross section and is discussed below, $\bar{q}$ is the equilibrium charge state in dilute gasses and is equal to the accelerated ion charge. If the value of $\sigma_s$ is known, then the value of $\sigma_p$ at the equilibrium point is known.

It is then assumed that the pickup cross section between these two points (Equations (9) and (5)) is given by:

$$\sigma_p \ (E) = \sigma_p \ (E \simeq o) \ e^{-\gamma E} \qquad (10)$$

$\gamma$ is the constant connecting the two points described above. Examination of the latest experimental cross section data[9,14,15] with this assumption reveals reasonable agreement for heavy ions of mass <150 amu.

Above mass 150, the predicted cross sections are less than the data by ≃ a factor of 3. Since masses above 150 amu, spend a large proportion of their acceleration history withing the charge pickup region, and in order to arrive at a conservative vacuum prediction for the MSU cyclotron, an empirical fit to the data has been derived. An empirical method of fitting the data point of Olson and Salop by adjusting the ion velocity for equation (6) yields an excellent fit to the uranium data as shown in figure 1. However, this fit as a function of mass (shown in figure 2 for a variety of charge states) predicts a value of the cross section that exceed the measurements by a factor of 3 for krypton. Therefore, the empirical fit has been used only for masses greater than 150 amu.

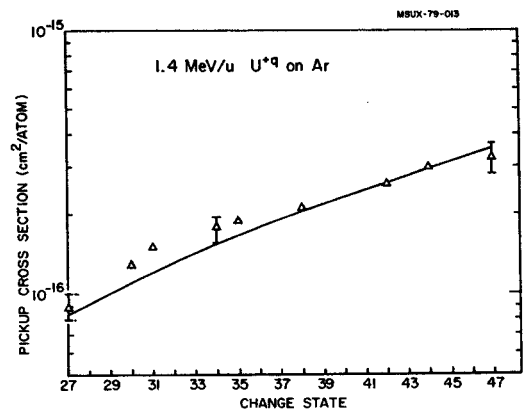


Fig. 1. The calculated charge pickup cross section for various charge state of uranium (solid line) are compared with the measured data at 1.4 MeV/u. The method for calculating the charge pickup cross section was adjusted to fit this data since the heavy mass ions in the acceleration process through the K500 cyclotron are spending more time in the charge pickup region and therefore can effect the required vacuum.

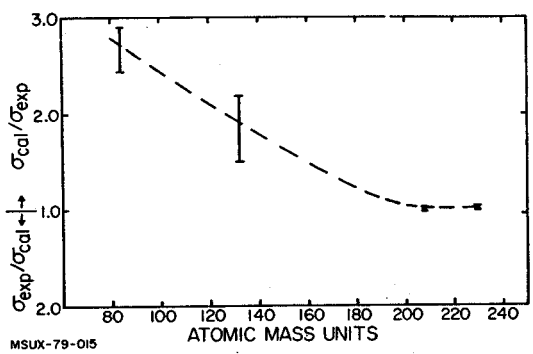


Fig. 2. The ratio between the calculated charge pickup cross section and the measured data at 1.4 MeV/u for Kr, Xe, Pb and u for various charge states are shown. The bar at each point represents the maximum ratio of the data for various charge states at that mass. The analytical method was adjusted so that the calculation best fitted the data at uranium where the accuracy of the method in predicting the vacuum requirements is more critical. The analytical method also gives a larger value than measured, so that the vacuum requirements will be on the conservative side.

b. Charge Stripping Cross Section

The charge stripping cross section has been divided into three regions of ion velocity where different analytical methods are assumed. For the low velocity regime, i.e. $v < 1.2\ v_e$, where $v_e$ is the velocity of the least bound electron of the projectile, the theory of Bohr-Lindhard[9,16] has been used and is the following:

$$\sigma_s = \pi a_o^2\ Z_T^{2/3} Z^{4/3}\ q^{-3}\ (v/v_o)^2 \qquad (11)$$

where $a_o$ is the Bohr radius ($5.291 \times 10^{-9}$ cm), $Z_T$ is the atomic number of the target atom and the other parameters have been defined.

At high velocity, $v > 1.2\ v_{ef}$[19], $v_{ef}$ is the most tightly bound electron of the projectile, the results of Gillespie, et al[17,18] have been used. Namely, they find that the cross section should decrease to first order by $(\beta^2)^{-1}$.

$$\sigma_s = \sigma_o/\beta^2, \qquad (12)$$

where $\sigma_o$ is the cross section at $v = 1.2\ v_{ef}$. For the region of $1.2\ v_e \leq v \leq 1.2\ v_{ef}$, $\sigma_s$ is set constant and is equal to the Bohr-Lindhard cross section obtained at $1.2\ v_e$. Unfortunately, very little data exist in the high velocity region to verify the above asusmptions. Figure 3 is the measured loss cross section for a $N^{5+}$ ion at high velocity. The solid line is the cross section obtained by the analytical procedure and gives an excellent fit to the data.

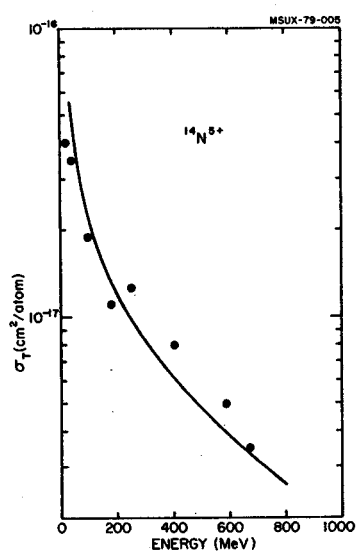


Fig. 3. The theoretical stripping cross section (solid line) for $^{14}N^{5+}$ at high velocity favorably compares with the experimentally measured values from the PPA (Circles).
The experimental cross section is the sum of all loss process ($\sigma_T$) and this is the cross section relevant for particle accelerator vacuum requirements. These experimental cross sections are presently the highest energy/nucleon heavy ion data available.

Using the above procedures, a numerical value for the beam loss cross section ($\sigma_L$) can be calculated for different velocities, ions, targets.

$$\sigma_L = \sigma_p + \sigma_s \ . \qquad (13)$$

In figure 4, $\sigma_L$ has been calculated for $N^{5+}$ using the various models. The points A,B,C, and D on the curves labelled MSU ($\sigma$p) and MSU ($\sigma$s) are the velocities where the analytical method has been modified as previously described. For this ion, the cross section obtained in these calculations are less than used by the Omnitron, but greater than used by the Unilac.

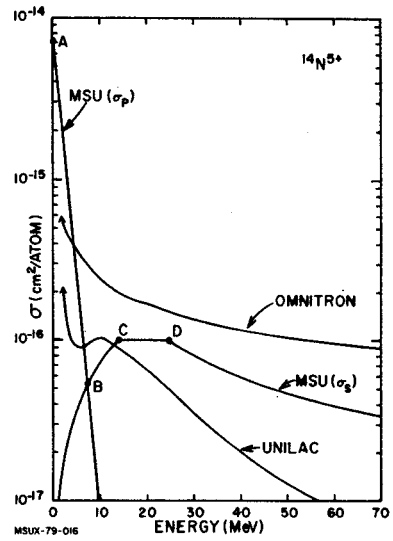


Fig. 4. The various theoretical cross section values used in vacuum calculation for the Omnitron (1966), the Unilac (1967) and the MSU superconducting cyclotron (1979), are shown for a $^{14}N^{5+}$ beam.
MSU ($\sigma_p$) is the value for the charge pickup cross section and MSU ($\sigma_s$) is the value for charge stripping. The points A-D indicate various decision points in our model and these are discussed in the text.

CYCLOTRON TRANSMISSION

The transmission calculations of the particle through the acceleration process is numerically integrated for each turn. The path length from equation (4) is given by the following equation for a cyclotron:

$$dl = 2\pi\left(\frac{2\ m\ E}{q^2\ B^2}\right)^{1/2}\ , \qquad (14)$$

where B is the cyclotron average magnetic field and m is the particle mass. The energy (E) of the particle is calculated for each turn and is the following:

$$E = E_o + \sum_{n=1}^{T} q\ d|V \cos\ (h\theta)|\ , \qquad (15)$$

where $E_o$ is the initial energy, d is the number of dees, V is the maximum dee voltage (isochronism is assumed), h is the rf harmonic number, $\theta$ is

the dee angle, and T is the number of particle orbits.

The majority of the calculations have assumed only one background gas specie, that being nitrogen or the gas used in the ion source. The variation of pressure versus radius has been assumed to be constant for the above calculation[21] and the transmission is calculated for a variety of pressure values. Figure 5 shows a typical transmission calculation for $^{40}Ar^{8+}$ as a function of energy, where the pressure has been varied from $5 \times 10^{-6}$ Torr to $1 \times 10^{-7}$ Torr and nitrogen background gas has been assumed.

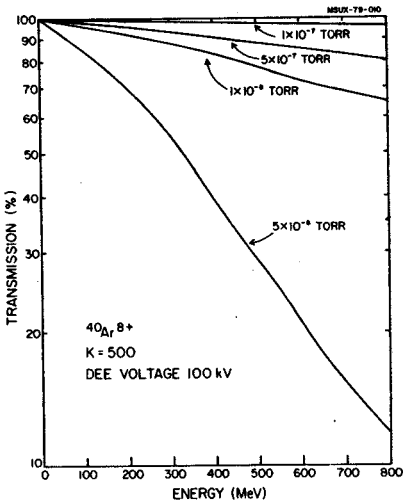


Fig. 5. The transmission curve for an $^{40}Ar^{8+}$ as a function of energy and for various pressures is shown for the MSU superconducting cyclotron. Greater than 90% transmission is expected for an acceleration vacuum of $1 \times 10^{-7}$ Torr.

## ACCELERATOR VACUUM CALCULATIONS

The previously described model has been used to calculate the beam transmission for various accelerators. The comparison of the predicted transmission with existing cyclotrons provides a valuable check upon the validity of the many assumptions. In particlular transmission calculations have been done and compared with experimental beams[21] from the 88" cyclotron at the University of California at Berkeley and the ORIC cyclotron at Oak Ridge National Laboratory. Figure 6 gives two examples from the 88" cyclotron. The experimental data has been normalized at 20 MeV to the calculations. The calculations predict a larger transmission loss than detected but the fit is considered to be good. The neon beam data has a large uncertainty on the pressure distributions since the 20K cryopanels do not pump neon gas. We also note that the calculation appears to be on the conservative design side for the vacuum requirements of a new accelerator for these measured

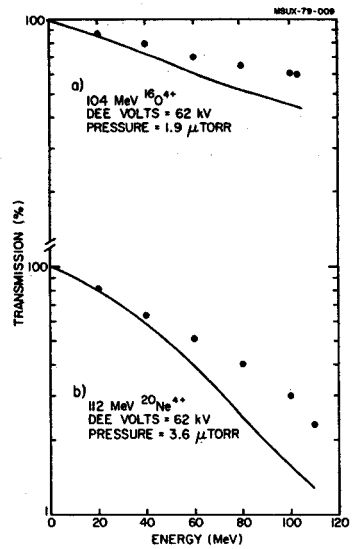


Fig. 6. Comparison of two theoretical and measured transmission curves for the 88" cyclotron at Berkeley, California, are shown. The calculations are solid lines which appear in good agreement with the measured data points (circles).

beams. Figure 7 is the transmission comparison of an $^{40}Ar^{4+}$ beam from the ORIC accelerator and the results are also considered to be in excellent agreement.

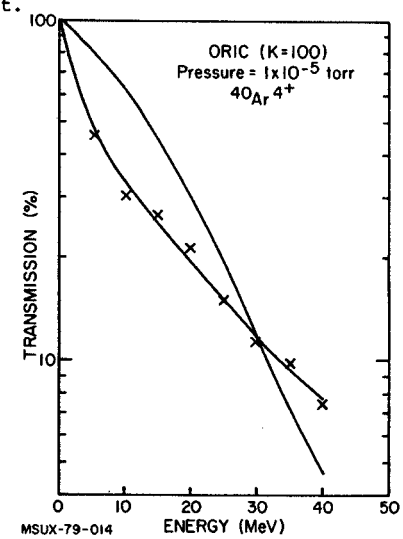


Fig. 7. The measured and calculated beam attenuation for a $^{40}Ar^{4+}$ beam on the ORIC cyclotron is shown. Before the vacuum calculation, the origin of these heavy ion beam losses were uncertain. The difference in the curves are consistent with the constant pressure assumption used in the calculations versus the real pressure in the cyclotron, namely higher at the center and lower at the extraction region.

The usefullness of these transmission calculations is well illustrated in figure 8, where the transmissions have been calculated for the Cern PS,[22,23] accelerator. In this machine, the beam make more than 7,000 turns and the path length is greater than 70kM. Trials at accelerating heavy ion beams at Cern are expected in the summer of 1979 and should provide an excellent check

on the calculation assumptions for the high velocity particles.

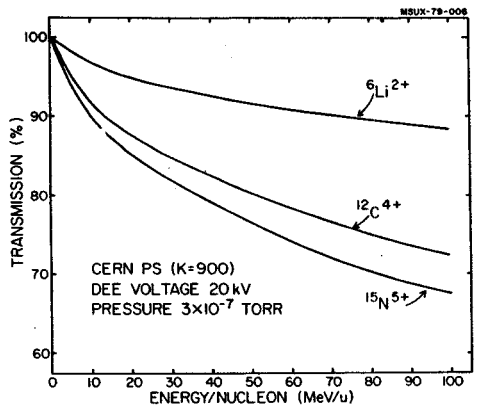


Fig. 8. The predicted transmission curves for three heavy ion beams on the Cern PS. The beams make more than 7400 turns and travel a distance greater than 70 KM. A large fraction of the beams for all three particles is predicted to be successfully transmitted to full radius for a pressure of 3 x $10^{-7}$ Torr and a dee voltage of 20 KV.

Figures 9 and 10 are some expected transmission values for the K500 superconducting cyclotron under construction at MSU. The two figures are for charge states +4 and +8 as a function of mass. A dee voltage of 100KV has been used and it is seen that the particles around atomic mass 40 are the most critical for determining the vacuum requirements. Greater than 90% transmission is expected for a vacuum of 1 x $10^{-7}$ Torr for all particles. The variation in the transmission as a function of mass, best illustrated in figure 9, is primarily due to the changing path length which is caused by the different charge to mass ratio and rf harmonic. For example, the masses at 130 amu in figure 9 are accelerated on a maximum voltage rf harmonic, thereby the beam's path length is decreased and hence the transmission is increased.

## SUMMARY

An analytical method for calculating the vacuum requirements of heavy ion cyclotrons has been described. This method involves matching the various loss cross sections over different velocity and mass regions to experimental and theoretical results.

Transmission calculations have been performed for existing heavy ion cyclotrons and are in good agreement, thereby confirming the validity of the cross section assumption over the range of comparison. Transmission calculations have been performed to predict the attenuation of heavy ion beams at the Cern PS and the vacuum requirement for the K500 at MSU. With the successful operation of the K500, the validity of the above method will be checked and make possible the extension of these calculations to future high energy heavy ion accelerators.

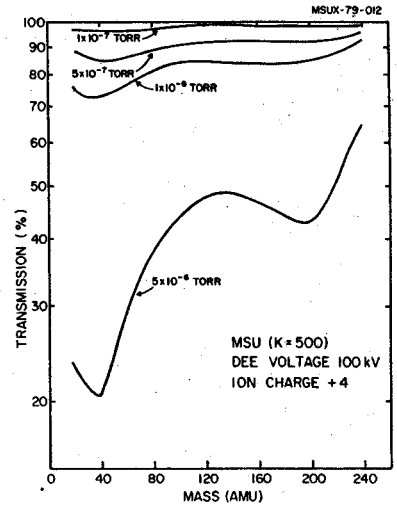


Fig. 9. The predicted transmission for ions with charge state four from the MSU (K500) superconducting cyclotron as a function of atomic mass is shown. The transmission was calculated for various pressures and greater than 90% transmission is predicted for a pressure of 1 x $10^{-7}$ Torr for all ions.

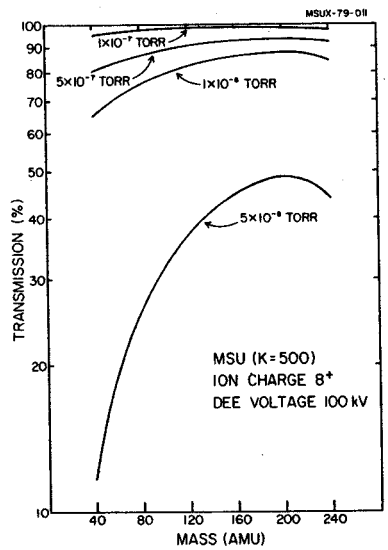


Fig. 10. The predicted transimssion for ions with charge state eight from the MSU (K500) superconducting cyclotron as a function of atomic mass is shown. A pressure of 1 x $10^{-7}$ Torr yields greater than 90% transmission for all ions.

1. E.J. Jones and K.J. Howard, Fifth International Cyclotron Conference, Butterworths, 200 (1971).
2. R.S. Lord, B.L. Duelli, E.D. Hudson, M.L. Mallory, E. Newman, M.J. Saltmarsh, W.R. Smith, S.S. Stevens, and A. Zucker, Fifth International Cyclotron Conference, Butterworth, 453 (1971).
3. E.D. Hudson, R.S. Lord, M.L. Mallory and P.H. Stelson, AIP Conference Proceedings, No. 9, Cyclotron - 1972, American Institute of Physics, 274, (1972).
4. E.D. Hudson, R.S. Lord, M.L. Mallory, J.E. Mann, J.A. Martin, W.R. Smith, IEEE TRANS. Nucl. Sci. NS-22, No. 3, 1544 (1975).
5. H.G. Blosser, IEEE TRANS. Nucl.Sci., NS-26, 2040 (1978).
6. D.J. Clark, Rutherford Laboratory, Harwell Cyclotron Group Design Note (CDN. 500-30-060) (1963).
7. A. Ghiorso, R.M. Main, and B.H. Smith, IEEE TRANS. Nucl. Sci. NS-13, No. 4, 280 (1966).
8. H.D. Betz, C. Schmelzer, Unilac 1-67 (1967).
9. H.D. Betz, Rev. of Mod. Phys., Vol. 44, No. 3, 465 (1972).
10. D.H. Crandell, M.L. Mallory, and D.G. Kocher, Phys. Rev. A., Vol. 15, No. 1, 61 (1977).
11. R.E. Olson and A. Salop, Phy. Rev. A, Vol. 14, No. 2, 579 (1976).
12. T.A. Carlson, C.W. Nestor Jr., N. Wassermann, and J.P. McDowell, At. Data 2 (1970) 63.
13. H.P. Betz, IEEE Trans. Nucl. Sci., NS-19, No. 2, 249 (1972).
14. W. Erb, B. Franzke, G.S.I. Darmstadt, Private Comm., to be published (1978).
15. J. Alonso, D. Dietrich, and H. Gould, 1979.
16. N. Bohr, and J. Lindhard, Kgl. Danske Viedenskab., Mat.-Fys. Medd. 28, No. 7, (1954).
17. G. Gillespie, Proceedings of the Heavy Ion Fusion Workshop held at Brookhaven National Laboratory, BNL 50769, 45 (1977).
18. G. Gillespie, Y. Kim and K. Ching, Phys. Rev. A, Vol. 17, No. 4, 1284 (1978).
19. G. Basbas, R. Rice and F.D. McDaniel, IEEE Trans. Nucl. Sci., NS-26, No. 1, 1177 (1979).
20. M.V. Isaila, K. Prelec, M.G. White, IEEE Trans. Nucl. Sci., NS-19, No. 2, 206 (1972).
21. R.A. Gough and M.L. Mallory, IEEE TRANS. Nucl. Sci. NS-26, 2384 (1978).
22. R. Giannini, P. Mandrillion, Proceeding of the 7th International Cyclotron Conference, Birkhouser, Basel 609 (1975).
23. J.H.G. Madsen and R.Giannini, Private Communication, (1979).

# Estimate of Electron-Loss Cross Sections at High Energies

F.D. Becchetti*

Recent Born-approximation calculations,[1] originally done as part of the U.S. heavy-ion fusion program, appear to be applicable to the calculation of electron loss from energetic heavy ions in typical residual gases ($H_2O$, $N_2$, $H_2$) in beam lines and experimental equipment. Such losses produce spurious charge states, beam-halo, and in extreme cases attenuate the beam. The latter has been discussed by Mallory et al.[2] for cyclotron beam losses.

The available calculations have been compiled and interpolated, and are conveniently displayed as a reduced cross section, $\sigma_o$, where $\sigma_{e\text{-loss}} = \sigma_o/\beta^2$. The results for $N_2$ are shown in Fig. 1. The cross sections for $H_2$ are typically x 10 smaller, but otherwise exhibit a similar behavior with q and Z. The interpolated cross sections are valid for ion velocities ($\beta = V/c$) greater than the orbital velocity of the stripped electron, or typically $\beta > 0.07$ for $q = 10^+$. The predicted cross sections have been checked against available data[3] and calculations[4] and generally reproduce these to x 3 or better, which is adequate for most purposes. (The behavior of electron capture and loss at low $\beta$ have been reviewed in several articles.[4,5,6])

A typical vacuum of $10^{-6}$ torr of $N_2$ results in an attenuation (and halo) of about $10^{-5}$ per meter of path length for $^{20}Ne^{6+}$ at E = 800 MeV, less for $H_2O$ and $H_2$, which are more typical gas components.

Most practical MSU phase-I beams (i.e., $\beta \gtrsim 0.15$, $E/A \gtrsim 10$ MeV/amu) will correspond to curves $q = 3^+$ to $7^+$ of Fig. 1, corresponding to attenuation and halo of $10^{-4}$ to $10^{-7}$ per meter for $P = 10^{-6}$ torr ($N_2$).

[NOTE: $T = \exp(-3.5 \times 10^{16}\, P(\text{torr})\,\sigma(\text{cm}^2)\,L(\text{cm}))$]

---

* On leave from University of Michigan, Ann Arbor, MI.


1. G. Gillespie et al., Phys. Rev. A17, 1284 (1978); BNL-50769 (1977), and private communication (1978).
2. M. Mallory, MSU Cyclotron Lab. Progress Report (1977); R. Gough and M. Mallory, Proc. 8th Intl. Cyclotron Conf. (U. Indiana, 1978).
3. J. Alonzo et al., private communication (1978); E. Baron and B. Delaunay, Phys. Rev. A12 (1975).
4. H.D. Betz and Ch. Schmelzer, UNILAC Report 1-67 (1967).
5. H.D. Betz, Rev. Mod. Phys. 44, 465 (1972); Methods of Experimental Physics, vol. 14 (1979) in press.
6. V. Nikolaev, Soviet Physics Usp. 8, 269 (1965).
7. B. Delaunay, Nucl. Inst. Meth. 146, 101 (1977).


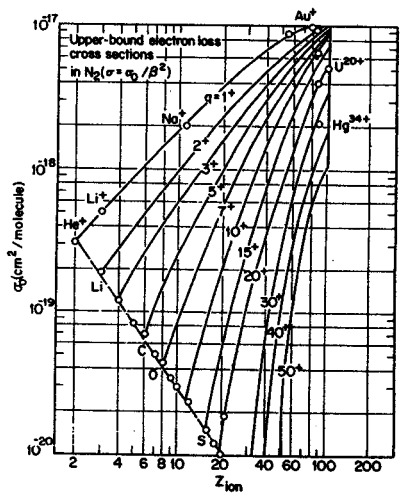


Fig. 1. Reduced cross sections, $\sigma_o$ ($\sigma_{e\text{-loss}} = \sigma_o/\beta^2$).

# Vacuum Tests Related to K = 500 Cyclotron Project

F.D. Becchetti* and J. Wilson

A number of tests have been performed relevant to the 1) design and operation of beam lines and experimental equipment (40 inch chamber and split pole magnet); 2) outgassing measurements of construction materials; and 3) tests of commercial and fabricated cryopumps (T = 4°K to 15°K). The results are described in detail in MSU internal reports, MSUCL-291, MSUCL-292, and MSUCL-
A typical high vacuum (P = $10^{-7}$ torr) outgassing spectrum for aluminum plate is shown in Fig. 1. One notes the dominance of water vapor in the spectra, which is typical of other materials. Pump down curves for a proto-type s.s. beam line section (Fig. 2) is shown in Fig. 3. Ultimate (gauge) pressures in the mid-$10^{-8}$ torr range appear feasible for beam line arrangements similar to that shown in Fig. 2.

*On leave from University of Michigan, Ann Arbor, MI.

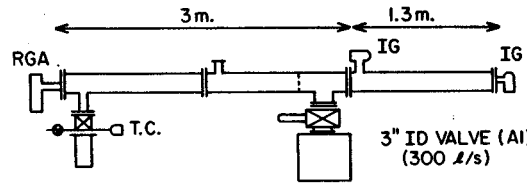


Fig. 2.

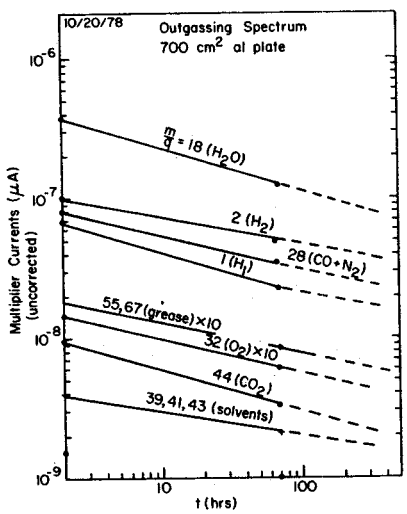


Fig. 1.

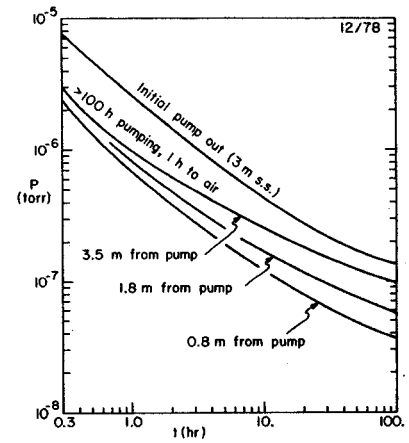


Fig. 3

## Survey of U.S. Heavy Ion Facilities

F.D. Becchetti*

A survey has been conducted of the major U.S. heavy-ion facilities with outside-user programs regarding typical utilization of experimental equipment. The results are shown in Fig. 1. The data displayed represent the fraction of time a piece of equipment, if available, is in use. Spectrometers appear to be the most utilized apparatus. Apparently many items are used only occasionally and thus could be placed together in a single beam room without many scheduling conflicts. Surprisingly, atomic physics and related fields encompass about 30% of the research effort at most laboratories and therefore must be considered in facility planning.

*On leave from University of Michigan, Ann Arbor, MI.

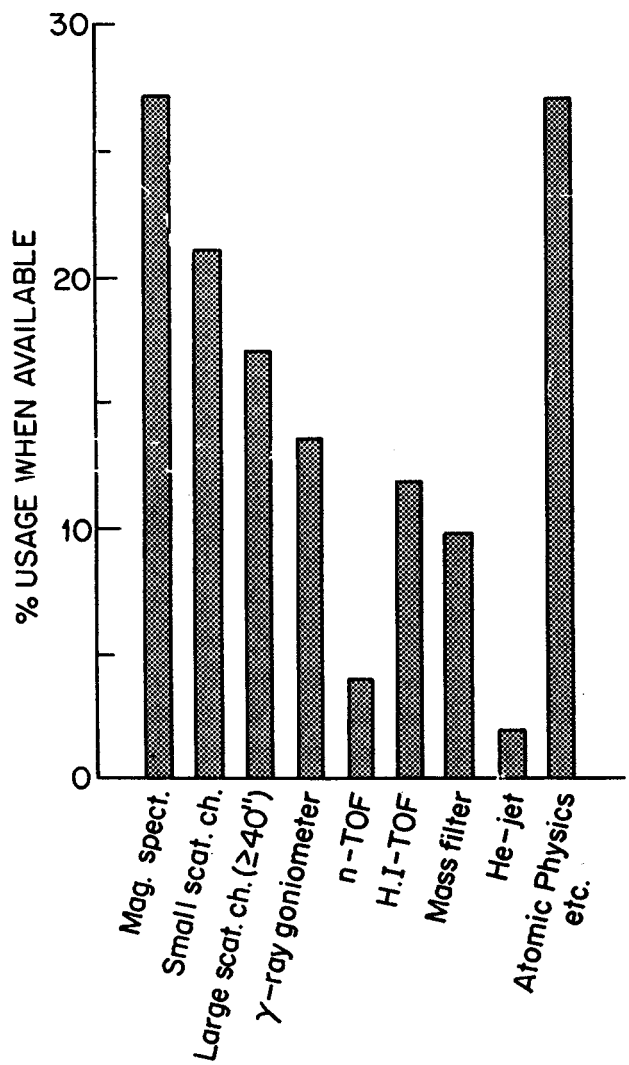


Fig. 1. Facility usage.

## Irradiation of Accelerator Materials With Energetic Heavy Ions

F.D. Becchetti*

Samples of 304 s.s., 6061 al., and other materials have been bombarded with 90 MeV $^{6}Li$ and 315 MeV $^{16}O$ at IUCF[1] and Texas A & M.[2] Absorbers were used for the latter irradiation to produce a range of $^{16}O$ energies (100 to 315 MeV). Residual activities were typically $\lesssim$ 100 mr/hr on contact per particle μC, 10 hrs after bombardment with $t_b \cong t_{1/2} \cong 1$ to 6 hours. Brass and stainless steel samples were typically x 3 more active than aluminum or carbon after 10 hours. The residual activity induced by $^{16}O$ appears to increase as $(E/A)^n$ with $n < 2$, i.e., with the range of the incident ion ($R \propto E^{1.7}$). The induced activity appears to increase slightly (x 2) for $^{16}O$ versus $^{6}Li$ at the same E/A.

The results appear to correlate with published neutron production measurements for energetic heavy ions[3] and can be extrapolated to estimate beam-induced activity expected for MSU Phase-I beams.

* On leave from University of Michigan, Ann Arbor, MI.

1. In collaboration with W. Jacobs (IUCF).
2. In collaboration with R. Rodgers (Texas A & M).
3. H. Patterson and R. Thomas, Accelerator Health Physics (AP, 1973) Chap. 3.